Ocean Engineering 311 (2024) 118804

Contents lists available at ScienceDirect

Ocean Engineering

journal homepage: www.elsevier.com/locate/oceaneng

Research paper

A fast simulation method for the probabilistic assessment of emissions in cruise ship's itinerary planning

Luca Braidotti *, Samuele Utzeri, Serena Bertagna, Vittorio Bucci

Department of Engineering and Architecture, University of Trieste, Via Valerio 10, 34127 Trieste (TS), Italy

ARTICLE INFO

Keywords:
Itinerary planning
Cruise ship
Emissions
Probabilistic approach
Environmental condition
Power management system
Fresh water

ABSTRACT

This study employs a probabilistic methodology to forecast cruise ship emissions during the itinerary planning phase, considering environmental factors (current, waves, wind), fouling, shallow water, loading conditions, and Fresh Water (FW) production effects. Probability distributions of environmental parameters are established based on statistical data and utilized for generating deterministic scenarios through Monte Carlo sampling. The resulting scenarios are simulated to define probability distributions for carbon dioxide emissions, carbon intensity indicators, and other pertinent quantities. The simulation model is validated using data from an existing ship. To demonstrate the effectiveness of the proposed methodology in strategic itinerary planning, multiple alternatives for an existing itinerary are simulated. Specifically, a Mediterranean cruise is simulated in both the original sequence and in reverse, with and without FW production. The reverse sequence without FW production demonstrates a potential reduction of approximately 190 tCO2e/week emissions. Furthermore, in this scenario, a comparison is made between a standard Power Management System (PMS) with an equal load on all engines and an optimized PMS with optimized engine loads, resulting in an additional average reduction of 86 tCO2e. In the latter itinerary, the most probable rating according to Carbon Intensity Indicator is reduced from original E to C.

1. Introduction

Following the interruption caused by the COVID-19 pandemic, the cruise market has resumed its growth, reaching rates comparable to those observed in the previous decade (Sucheran, 2021; Lin et al., 2022). Despite the increasing demand, the cruise industry is anticipated to encounter several challenges in the near future, primarily driven by the imperative of decarbonization. Stringent international and European regulations are compelling cruise companies to implement measures aimed at reducing emissions from their ships (Ancona et al., 2018; Lindstad and Rialland, 2020; Bertagna et al., 2023). Specifically, the International Maritime Organization (IMO) has introduced the Energy Efficiency Existing Ship Index (EEXI) and the Carbon Intensity Indicator (CII) to steer efforts towards achieving net-zero emissions by 2050 (IMO, 2023b). Additionally, the European Union, through the Fit for 55 regulation (European Commission, 2021), has mandated shipping companies to progressively purchase and surrender emissions allowances on the European Emissions Trading System (ETS). Consequently, the imperative to reduce emissions is no longer merely ethical but is now driven by mounting economic pressures.

In this context, significant strides can be made by designing new itineraries with a lower environmental footprint. Cruise companies start itinerary planning at a strategic level years before their actual deployment. This process involves a delicate balance between environmental, technical, commercial, and economic factors, aiming to minimize environmental impact while selecting the most profitable option for the shipping company. The main objectives of itinerary planning, given a specific itinerary, include assessing the technical feasibility of all legs/calls and evaluating overall itinerary performance (environmental, technical, economic). This work primarily focuses on the environmental aspect, which is inherently correlated with the others. An itinerary must be technically feasible, and emissions are predominantly driven by fuel consumption: the second-largest expenditure for cruise ships (after crew wedges) and the most susceptible to uncertainty. Moreover, cruise ships exhibit a peculiarity compared to other vessels concerning Fresh Water (FW). On cruise vessels, FW consumption surpasses fuel consumption by an order of magnitude, significantly impacting the loading condition or necessitating onboard production means that affect emissions due to their electric energy demand.

The forecasting of fuel consumption, FW consumption/production, and the associated emissions is inherently a probabilistic problem. This is due to their dependence on various factors, including environmental conditions (waves, wind, current, season, etc.), the number

* Corresponding author.
E-mail addresses: lbraidotti@units.it (L. Braidotti), samuele.utzeri@phd.units.it (S. Utzeri), sbertagna@units.it (S. Bertagna), vbucci@units.it (V. Bucci).

https://doi.org/10.1016/j.oceaneng.2024.118804
Received 19 April 2024; Received in revised form 24 June 2024; Accepted 22 July 2024
Available online 5 August 2024

of persons onboard, and the human factor, which encompasses how the ship and its main systems are operated. Cruise companies employ various approaches to forecast the fuel consumption of a ship during itinerary planning, ranging from design data provided by the shipyard to historical data from previous years of ship operation. However, historical data are often affected by human errors in main systems' operation (Vasilikis et al., 2022): if not properly utilized, generators and main machinery could involve higher energy absorption than design values. Furthermore, applying purely data-driven approaches may fail to capture and model the behaviour of complex systems, such as the ship propulsion system, chiller units, etc. On the other hand, design data provided by the shipyard can lead to optimistic predictions, as they are based on predefined design conditions that do not account for actual environmental conditions and fouling accumulation, both of which strongly impact ship emissions (Uzun et al., 2019).

These considerations advocate for the adoption of physical simulation models (white-box or, possibly, grey-box capable of accurately modelling the complexities of cruise ship systems based on the values of several stochastic variables. Such models can simulate ideal ship operation in realistic environmental conditions while applying consistently all the cruise companies' procedures and requirements about machinery and systems operation and voyage schedule, thereby removing possible disruptions due to human factors. Shipping companies are committed to accurately assessing emissions and fuel consumption during itinerary planning. However, incorporating human factors in this assessment, while providing a more realistic prediction of the status quo, is not considered beneficial by cruise company management. It might encourage the adoption of incorrect behaviours in ship operation (such as keeping an excessive number of diesel generators running), leading to increased fuel consumption and, consequently, emissions. Hence, planned itineraries should be regarded as a realistically ideal scenario, serving as a target for the ship's crew through respecting the itinerary schedule (i.e. speed) while operating machinery and systems according to company recommendations and procedures. Moreover, the computational effort required for simulations should be minimized to provide cruise management with not only informative results but also reasonably fast responses during itinerary planning, where multiple alternatives are usually considered. Hence, high-fidelity tools such as fully dynamic time-domain simulations and computational fluid dynamics, cannot be directly applied in this phase suggesting the application of simplified physical simulation methods.

Currently, several simulation models are present in the literature, as will be discussed extensively later on. However, none of them is specialized for cruise ships which are usually more complex to operate compared to other merchant or naval ships. Besides, in the literature, only a few works such as Ambrosino and Asta (2021) addressed the cruise itinerary planning phase. None of them accounts for the environmental aspects or adopts a probabilistic approach, using very poor methods to estimate fuel consumption. Hence, there is a gap in the literature concerning itinerary planning for cruise ships, although major cruise companies are showing increasing attention in this critical phase.

To address such a market need, this work presents a simulation model of a cruise ship developed for itinerary planning, capable of predicting the probability distributions of emissions and the probability of achieving a CII rating. The novelty of the work is twofold: first the formulation of a probabilistic approach to the emissions assessment applicable during the itinerary planning; second, the development of a deterministic physical simulation model specialized for cruise ships, requiring a limited number of input data already owned by cruise companies to foster its fast application. The proposed methodology considers seasonal weather conditions during navigation using wave, wind, and current statistics, manoeuvring phases (entering and leaving a port), and the electric load at berth. It does not include human factor, providing an ideal benchmark for cruise operations. The potential of the proposed technique in itinerary planning is showcased by comparing four one-week itineraries calling the same ports, with variations in sequence (original and reversed) and FW production (active in navigation or disabled). Furthermore, the itinerary with the lowest emissions is also simulated, considering an optimized load on diesel generators as opposed to the current practice of an equal distribution of load. This illustrates the capability of the proposed technique to evaluate enhancements in the setup and operation of onboard main machinery.

The remainder of the paper is organized as follows. In Section 2 a literature review is provided to deeply discuss the research gap and need for a novel comprehensive approach applicable to cruise ship itinerary planning. Section 3 provides the proposed methodology focusing on assumption and data sources, adopted simulation process, assessment of ship heading and resistance, and emissions assessment. In Sections 4 and 5 the test ship and test itineraries are presented, respectively. In Section 6 the results related to PMS maps, validation of the deterministic model, sensitivity analysis on the number of scenarios and probabilistic simulations are provided, while they are discussed in Section 7. Section 8 summarizes the main conclusions of the study and future work needed to improve the proposed methodology.

2. Literature review

Several simulation models found in the literature aim to assess emissions (Bouman et al., 2017; Nunes et al., 2017) and/or fuel consumption of ships (Fan et al., 2022). These methods are primarily used to solve two types of problems that require a large number of individual simulations for their operation:

- Emission inventory at the global, regional, or local scale,
- Weather routing, which typically aims to minimize fuel consumption (and consequently emissions).

For both types of problems, the adopted simulation techniques can vary significantly, focusing on different aspects of the same problem with the appropriate level of detail.

Emission inventory typically involves the reanalysis of a large number of ships, with only limited technical data available (usually public information from class societies or other sources). Therefore, it is conducted after the studied event based on historical datasets. In this context, two main approaches can be adopted: the top-down or the bottom-up approach.

The top-down approach estimates pollutant emissions based on the amount of bunkered fuel (Merien-Paul et al., 2018). Conversely, the bottom-up approach (Schwarzkopf et al., 2021) is based on the reanalysis of maritime traffic, both in ports and during navigation, utilizing the Automatic Identification System (AIS), which collects historical data on speed, heading, and environmental parameters (Johansson et al., 2017). In such cases, a physical simulation model is needed to assess the actual fuel consumption and related emissions based on the known route and environmental conditions. This process must be repeated for a large number of ships, which increases with the geographical region under analysis.

In weather routing, weather forecasts can be used to optimize the speed and route of a specific vessel with a particular position and destination at a specific time (Zis et al., 2020). This problem is related to a single ship, for which the optimization has to be performed immediately before departure and/or adjusted during the voyage according to short-term weather forecasts. Therefore, the environmental conditions are usually fixed (Simonsen et al., 2015) or subject to some uncertainty (Kepaptsoglou et al., 2015), while multiple ship routes are inherently considered in the optimization process. If an ensemble method is used to capture weather forecasts uncertainties (Sandvik et al., 2021; Vettor and Guedes Soares, 2022; Jeuring et al., 2024), multiple scenarios can be generated also in solving weather routing problems by introducing perturbations on initial conditions of the employed model. These methods can be used also in hindcasting of wind and wave conditions to quantify the model error, study extreme

Table 1
Comparison of different problem statements highlighting their differences from itinerary planning.

	Emissions Inventory	Weather routing	Itinerary planning
Number of ships	Multiple	One	One (or multiple if a fleet is considered)
Ship route	One (historic record)	Multiple (variable of the problem)	Multiple (alternative itineraries under study)
Environmental condition	One (historic record)	One (short-term weather forecast)	Multiple (matching historic probability distributions)
Execution	After fleet voyage	Days-hours before ship voyage	Years before ship voyage

events or increase the sample size for statistical studies (Osinski and Radtke, 2020).

The problem addressed in this study differs significantly from previous ones as summarized by Table 1. It aims to forecast the most probable outcomes of a proposed itinerary and the probability distributions of its main performance indicators (e.g. fuel consumptions, emissions) well in advance. This task is incompatible with relying on weather forecasts, even if an ensemble method is applied. In fact, weather forecasts cannot give any insight about expected weather conditions one or two years in advance. Nonetheless, this is the time frame between itinerary planning and itinerary deployment. Therefore, statistical modelling of hindcast data is necessary for all relevant environmental parameters, as proposed in Kuroda and Sugimoto (2022) for cargo ships, focusing solely on added resistance. Consequently, the new problem addressed by the proposed methodology entails simulating multiple scenarios based on probability distributions for all pertinent environmental factors, while considering a single ship operating along a specific route, i.e. the itinerary under analysis.

Currently, there is no comprehensive method in the literature for predicting the impact of environmental factors on a specific route using a probabilistic approach, despite its necessity for accounting for environmental conditions in itinerary planning. As mentioned, for this task, among the available methods, those requiring time-domain simulations such as Kobayashi et al. (2015), Donatini et al. (2019), Fan et al. (2020) or numerical techniques such as Tadros et al. (2022) are unsuitable due to their prohibitive computational demands. Usability, fast set-up and fast response are key elements, especially if the simulations are conducted in a business environment instead of an academic one. Consequently, simplified methods are typically employed to simulate ship behaviour in tasks requiring a large number of simulations (e.g. both emissions inventory and weather routing).

For instance, Toscano and Murena (2019) employed the top-down method to study emissions in ports based on maritime traffic of cruise and merchant ships. Simplified regressions for various pollutants such as sulphur oxides (SO_x) and nitrogen oxides (NO_x) during manoeuvring and berthing phases in ports were defined, considering consumptions attributed to hotel loads. However, the lack of reliable data on fuel quantities bunkered during port stays (Fuentes García et al., 2022) complicates the application of the top-down method, which proves effective when complemented with emission analyses during navigation. The fourth IMO GHG study (IMO, 2020) utilizes, in addition to the top-down method, a bottom-up approach. The use of AIS tracking systems (Woo and Im, 2021) allows for the identification of instantaneous speed, heading, and draft to employ power estimation methods, as done by the Maritime Transport Environmental Assessment Model (mariTEAM) by Bouman et al. (2016), Muri et al. (2019). This method, based on fleet power estimation for different ship types, calculates calm water resistance using various empirical methods (Holtrop et al., 1982; Van Oortmerssen, 1971), considering corrections for air resistance (Kitamura et al., 2017), added resistance (Liu and Papanikolaou, 2020), and fouling on the propeller and hull (Tadros et al., 2023; Kytariolou and Themelis, 2023), which lead to significant increases in resistance. Although being a reliable tool for the estimation of overall emissions on a large fleet with limited technical information, this approach might be too simplistic when applied to a single vessel since it does not account for corrections due to ship true heading, current, shallow water phenomena, interactions between propeller, rudder, and additional resistance due to the presence of stabilizing fins in rough sea conditions. Moreover, the estimation of fuel consumption is obtained with a simplified algorithm based on load factors (Kramel et al., 2021), which, for complex diesel–electric systems used on cruise ships, may result in low accuracy due to human error in selecting active generators. Similar issues have been observed for naval ships by Vasilikis et al. (2022).

As noted earlier, weather routing typically employs simplified simulation algorithms, although shipowners usually have more information available about the vessel under study compared to the public data used in emissions inventories (but still incomplete compared to shipyards). This simplification aims to manage the computational burden of the optimization process, crucial for weather routing's operational use (Simonsen et al., 2015). For instance, Zaccone et al. (2018) presented 3D programming methods to select a route and speed profile based on meteorological maps for optimizing fuel consumption, taking into account ship motions and passenger comfort. However, this model neglects all environmental aspects other than sea state and wind. Advancement can be seen in Kytariolou and Themelis (2023), where a genetic algorithm is used to optimize fuel consumption for orthodromic or loxodromic routes. This approach considers the effects of fouling and current in addition to sea state and wind. Nonetheless, current effects are addressed in a very simple cinematic manner, and the model still does not account for the ship's true heading, shallow water phenomena, interactions between propeller and rudder, and additional resistance due to the presence of stabilizing fins in rough sea conditions.

An enhancement to these simulation models could be achieved if historical operational datasets were available for a single ship (Wang et al., 2022). In such cases, Black Box Methods (BBM) or Grey Box methods (GBM) could be considered. BBM utilizes statistical models and machine learning tools, such as regressions or neural networks, to directly estimate fuel consumption from a data sample based on a set of variables. Thus, given a new set of variables' values, the black box can estimate the response (e.g., emissions, fuel consumption, etc.). GBM are a hybrid solution employing physical methods combined with components based on machine learning. The main drawback of these approaches, apart from the need for data collection and storage facilities as prerequisites and the lengthy setup and training time, is the quality of the data. Specifically, the data may contain human errors that cannot be easily detected without the aid of a physical simulation model (Fan et al., 2022). This issue might be limited on merchant ships with simple propulsion systems using two-stroke engines and limited electric loads for other users, but it may not be acceptable for a cruise ship, where improper operation of the main machinery could significantly increase fuel consumption. Hence, while BBM and GBM may provide accurate estimates of the status-quo, they cannot establish reliable targets for the crew.

All these considerations underscore the importance of adopting a physical model with multiple Degrees of Freedom (DoF), as previously introduced by Tillig and Ringsberg (2019) for merchant ships. However, the literature has given very little attention to cruise ships, which have several peculiarities compared to other types of vessels (which will be discussed in detail later). None of the simulation models described in the literature have incorporated external air conditions

into the set of considered environmental factors, despite their notable influence on the power demand for air conditioning (Baldi et al., 2018). Only (Ambrosino and Asta, 2021; Asta et al., 2018; Ambrosino et al., 2019) addressed the problem of cruise ship itinerary optimization at a strategic level, with a primary focus on commercial and economic considerations. However, these studies have greatly oversimplified technical aspects, making it impossible to achieve an accurate estimation of the impact of environmental conditions and, consequently, operating costs. Hence, the literature review highlights the need for a comprehensive probabilistic method applicable to cruise ships, with immediate practical application in itinerary planning.

3. Methodology

In the present section, the applied methodology is presented in detail starting from the main assumptions and adopted data sources. Then the overall simulation process is discussed, detailing the most important steps.

3.1. Assumptions and data sources

In pursuit of strategically planning cruise itineraries through a probabilistic approach, this study introduces various simplifying hypotheses and assumptions to model the itinerary, the loading condition of the ship, its power system, and environmental conditions. These simplifications are instrumental in facilitating the execution of a considerable number of simulations at a reasonable computational cost. Subsequently, the primary assumptions, along with the utilized data sources, are elaborated upon.

3.1.1. Itinerary modelling

In the present study, the cruise itinerary of the ship is modelled through legs that connect one port to another. These legs are further subdivided into sublegs, representing straight segments characterized by constant ship speed, heading, loading condition, adopted fuel type, and environmental conditions. Each subleg is categorized as follows:

- **Navigation:** During this phase, the ship operates at or close to cruise speed in open or shallow waters.
- **Transit:** This phase occurs as the ship approaches a port, moving at a relatively low speed in restricted or shallow waters to reach the berth.
- **Manoeuvring:** This phase encompasses the ship's approach to the berth for mooring, during which bow and stern thrusters are active.
- **Port stay:** In this phase, the ship is moored at the berth with no propulsion service.

3.1.2. Loading condition

On a navigating ship, consumables influence the displacement and, consequently, the floating position. The vessel is assumed to maintain an even trim, but the actual loading conditions are considered to determine the actual draught T. The loading condition of a cruise ship is heavily affected by the procedures and standards applied for bunkering/resupply or the statistics from previous voyages. This is why the following assumptions have been defined in close interaction with a major cruise company in order to reflect their actual procedures regarding bunkering, and resupply and to benefit from their historic datasets for modelling passengers/crew occupancy and consumables consumption.

It is important to note that modern cruise vessels can utilize various types of fuel, including Marine Gas Oil (MGO), High Sulphur Fuel Oil (HSFO), Very Low Sulphur Fuel Oil (VLSFO), and Liquefied Natural Gas (LNG). Consequently, ships are equipped with dedicated tanks for each type of fuel. The choice among them is often not discretionary but mandated by international/local regulations. As per common practice in cruise ship operations, fuel can be bunkered at each port if necessary. Therefore, in this study, bunkering of a specific fuel type is automatically executed upon departure from each port when the filling factor of dedicated tanks falls below 30%. The tanks are then refilled up to 75%. Due to this customary practice, filling factors at the initial port of the itinerary are randomly assigned for each fuel type within the range from 30% to 75%.

Table 2
Passenger and crew occupancy ratio and related standard deviation.

	At Sea	At Berth
mean pax occupancy	0.93	0.63
pax occupancy st. dev.	0.02	0.03
mean crew occupancy	0.98	0.82
crew occupancy st. dev.	0.01	0.01

In addition to fuel, which significantly impacts every vessel type, the handling of Fresh Water (FW), grey water (GW), and black water (BW) on cruise ships must be considered to accurately define the loading condition. Indeed, FW tanks typically have a capacity comparable to fuel tanks on large cruise ships. FW can be procured at almost every port (at varying rates) and/or produced onboard using evaporators (utilizing heat recovered from engine cooling systems and electric energy) and/or reverse osmosis machines (which rely on electric energy). Here, ship operations can be simulated with or without freshwater production. Regardless, FW production is only performed during navigation phases, and an automatic FW bunkering policy is enforced if the level falls below 40% at departure. In such cases, FW tanks are replenished up to 75%. FW consumption is modelled based on an average consumption rate representative of a Mediterranean cruise, amounting to 0.24 t/(person day) for all individuals on board (passengers+crew). Consumed FW is then transformed into GW and BW, which are retained onboard in Grey Black Water (GBW) tanks, except during navigation phases when GW can be discharged at sea after treatment. In the latter case, 10% of treated water is still retained onboard to account for treatment residuals. When the filling factor of GBW tanks exceeds 70%, BW is discharged in port upon departure, leaving a residual 20% of tank capacity onboard.

In a well-designed itinerary, a cruise ship constantly carries near the maximum number of passengers (full payload) and nearly all nominal crew members during navigation, transit, and manoeuvring. In port, passengers and some crew members disembark. According to statistics applicable to the Mediterranean cruise scenario, all probability distributions of passenger and crew member occupancy ratios are assumed to be Gaussian, with mean values and standard deviations as reported in Table 2. Following Monte Carlo (MC) generation, passenger numbers resulting from generated occupancy ratios are rounded to the nearest integer and constrained within the range from 0 to the maximum number.

The current loading condition is assessed at the commencement of each subleg of the itinerary, and the bunkering/discharge of Grey Black Water (GBW) occurs solely upon departure from a port. This assumption adopts a conservative approach, as fuel is consumed and treated Grey Water (GW) is discharged at sea during navigation phases. This practice results in a gradual reduction of the ship's displacement and, consequently, its resistance.

3.1.3. Cruise ship power system

In this study, the ship's power system is modelled as illustrated in Fig. 1, which also presents the adopted nomenclature for powers and efficiencies. This layout is representative of modern cruise ships equipped with a diesel–electric propulsion system. The system embeds fixed-pitch propellers, typically two, driven by Propulsion Electric Motors (PEM). Electric energy, denoted as P_{el}, is supplied by the onboard power plant comprising diesel generators, usually ranging from four to six, located in two independent engine rooms. These generators are connected to

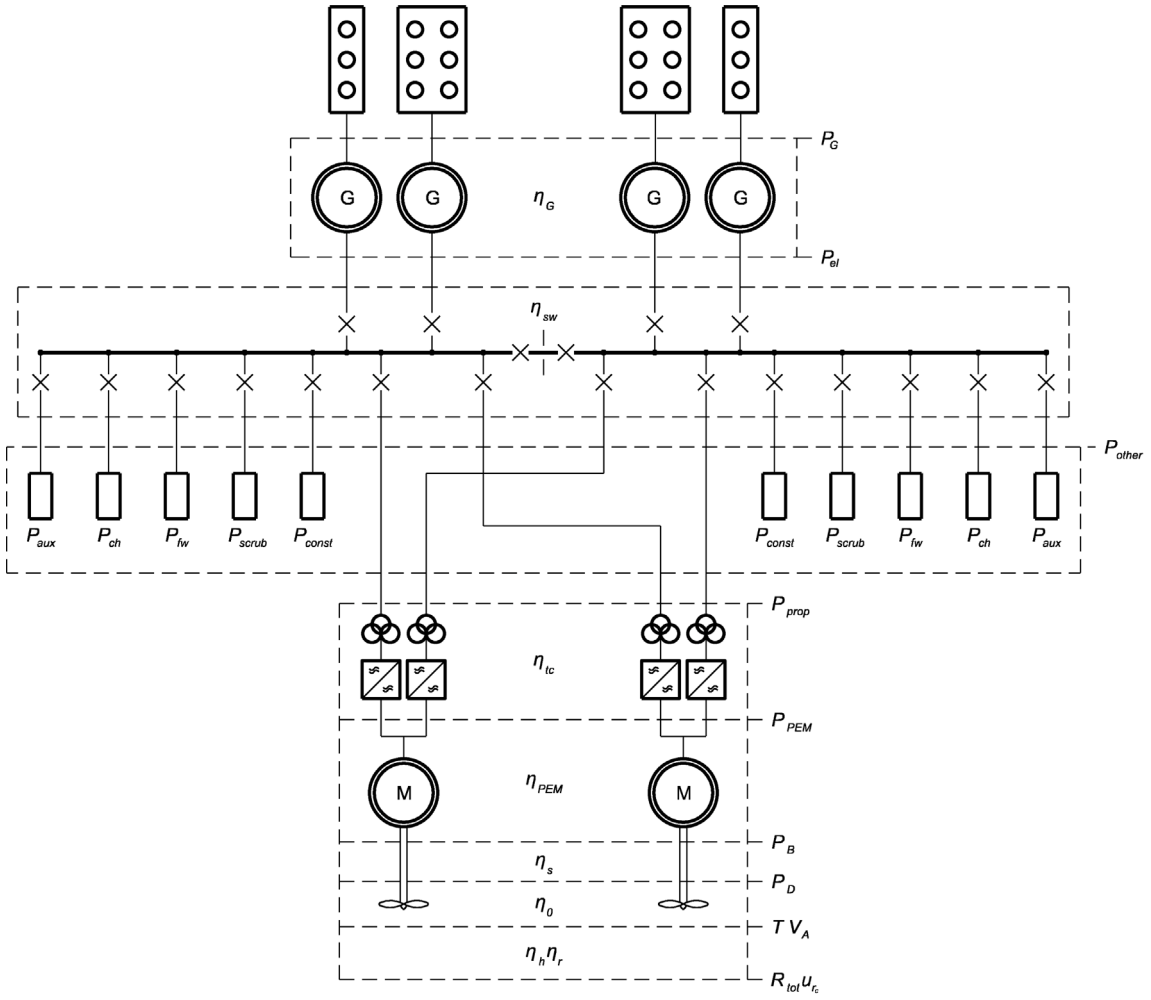

Fig. 1. Ship's power electric system.

the main switchboards of the ship. The switchboards distribute power P_{prop} to PEMs through electric transformers and converters, as well as to all other consumers denoted as P_{other}. In the context of a cruise ship, auxiliaries, and air conditioning represent the second and third energy absorbers after propulsion, and thus, their power demands are, here, considered not constant and addressed separately. The power demand for auxiliaries (P_{aux}) is defined as a bilinear function of the remaining overall power demand obtained excluding auxiliaries as ($P_{noaux} = P_{prop} + P_{other} - P_{aux}$). Additionally, the loads associated with air conditioning chillers (P_{ch}) are modelled as functions of the external air temperature T_a. Other electric loads detailed in the simulation model include those related to Fresh Water (FW) production (P_{FW}), as it can be deactivated based on phase or simulation requirements, and those associated with scrubbers (P_{scrub}), which are inactive in MGO or VLSFO mode. The values of P_{fw} and P_{scrub}, along with the remainder constant power P_{const}, are extracted from the ship's electric balance. All other loads and efficiencies are sourced from datasheets and documentation of the main machinery and electric equipment.

3.1.4. Environmental data

Environmental data for constructing probability distributions in Monte Carlo (MC) sampling are gathered from various sources. Initially, probability distributions of sea states are acquired from Hogben et al. (1986), offering sea scatter diagrams for nearly every global region. These reports delineate the likelihood of encountering a sea state characterized by the significant wave height $H_{1/3}$ and zero-crossing period T_z across 8 wave directions δ, in all four seasons. In this context, to randomly generate via MC sampling a generic deterministic scenario the following process is utilized. First, the 8 scatter diagrams for a specific area and season are selected according to the location and date of the itinerary to be simulated. Then, the cumulative density function of the wave direction $cdf(\delta)$ is defined fitting the 8 known values associated with the directions given by Hogben et al. (1986). Thus, the randomly generated wave direction is given by:

$$\delta_r = cdf^{-1}(rnd) \tag{1}$$

where rnd is a random number in $[0, 1]$ interval. Then, the scatter diagram containing δ is selected and for further processing. The cumulative joint probability distribution $cdf(T_z, \delta_r)$ is fitted using the 11 values of T_z reported in the selected scatter diagram. Using the same approach in Eq. (1), the random zero crossing period T_{z_r} is assessed. Finally, the empirical cumulative joint probability distribution $cdf(H_{1/3}, T_{z_r}, \delta_r)$ is defined using only the 15 probabilities related to $H_{1/3}$ reported in the scatter diagram column whose T_z interval contains T_{z_r}. The random $H_{1/3_r}$ is defined with the same approach defined in Eq. (1). With this process, generated random triplets $\delta_r, T_{z_r}, H_{1/3_r}$ representative of a sea state are consistent with the original statistic data from scatter diagrams.

The wind is assumed to be correlated with the sea state, with the wind direction γ considered identical to the wave direction ($\gamma = \delta$). Hence, it is implicitly assumed that wind has generated the random sea state. Wind speed V_w is calculated as a function of $H_{1/3}$ based

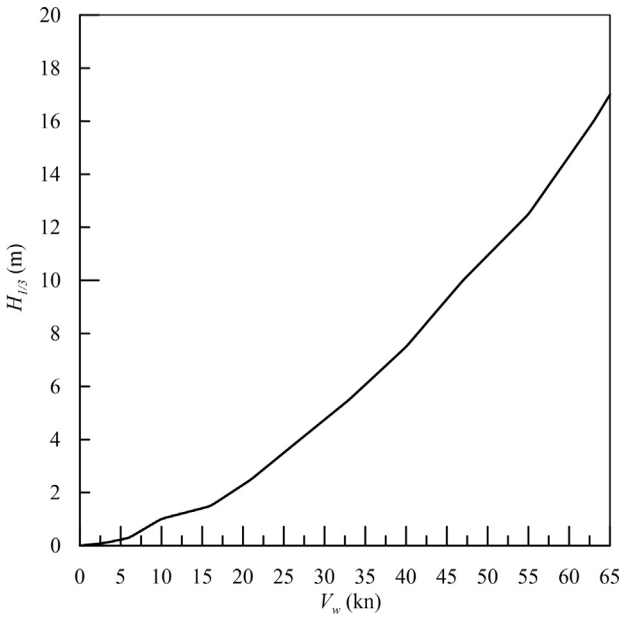

Fig. 2. Wind–wave relation according to Beaufort scale.

on the Beaufort scale as shown in Fig. 2. It shall be noted that this assumption introduces some inaccuracies especially in swell cases (that cannot anyway be identified among the random sea states since Hogben et al. (1986) does not distinguish between local wave pattern and swell.

Monthly average sea current speed V_c and direction β are assessed following Pilot Charts (NGIA, 2024), which provide monthly average speed and direction of the ocean currents in every area of the world. To model uncertainties on these average values, Gaussian noise is introduced in each randomly generated deterministic scenario, assuming a standard deviation of 0.03 kn for V_c and 5 deg for β. Current and other environmental data are treated as uncorrelated, discarding wind-induced and tidal currents.

The probability density function for the average daily air temperature $pdf(T_a)$ is defined through kernel fitting using observations from the past ten years. Kernel function is defined as:

$$pdf(x) = \frac{1}{nh}\sum_{i}^{n} K\left(\frac{x - x_i}{h}\right) \tag{2}$$

where x is the random variable, $x_1, \ldots, x_n$ is the data sample, K is the normal smoothing function (Kotz and Balakrishnan, 1993) and h the bandwidth given by:

$$h = \sigma\left(\frac{4}{3n}\right)^{1/5} \tag{3}$$

where σ is the standard deviation of the sample (Bowman and Azzalini, 1997). With this process, a cumulative probability density function $cdf(T_a)$ is established for each month under consideration. The same approach defined in Eq. (1) is used for the generation of a random value from the $cdf(T_a)$. Air temperature and other environmental data are presumed to be uncorrelated. Air density is computed as a function of T_a, assuming a pressure of 101.325 kPa.

Sea salinity (sa) and sea surface temperature (SST) are considered as consistently averaged values. These values are determined on a monthly basis using statistical data from the preceding ten years, which is sourced from Intergovernmental Oceanographic Commission (2010), and kept constant on all the randomly generated deterministic scenarios. Sea density ρ_w and kinematic viscosity ν_w are evaluated as functions of SST and sa following McDougall et al. (2003), Roquet et al. (2015).

3.2. Overall simulation process

The proposed methodology is inherently probabilistic and is illustrated in Fig. 3. To forecast fuel consumption and emissions for a given itinerary modelled through legs and sublegs, a multitude of deterministic scenarios is generated via Monte Carlo (MC) sampling. This is done based on probability distributions of stochastic variables (e.g., environmental conditions, number of passengers/crew members) as defined in Section 3.1. All stochastic variables are assumed to be constant along the leg (from port departure to the next port departure) except for the current direction and speed, which are assumed constant on each subleg instead of on the whole leg (sublegs shall be properly defined in order to be consistent with this hypothesis). Each deterministic scenario is then simulated to obtain the deterministic values of all the dependent variables $\mathbf{y}$ under study (e.g., fuel consumption, Fresh Water (FW) production/consumption, emissions, etc.). In the post-analysis phase, statistical measures such as the mean, median, and third quartile of the dependent variables are computed, along with their empirical cumulative distribution functions ($cdf(y_i)$). The $cdf(y_i)$ functions can be fitted using a kernel function, as for Eqs. (2) and (3) (Johnson et al., 1995; Bowman and Azzalini, 1997), to derive the probability density functions ($pdf(y_i)$).

The heart of the process lies in deterministic simulation, which provides the data necessary for constructing the probability distributions of dependent variables. The subsequent sections elaborate on the most relevant steps of the process, with a specific emphasis on propulsion systems and their electric load, since their typical contribution ranges from 1/2 to 2/3 of the onboard power demand during navigation.

3.3. Actual heading and total resistance evaluation

For a subleg of the itinerary with a length d_l, the ship is considered to move at a constant speed over the ground V_l along the direction α of the leg (true course). Nevertheless, to counteract environmental forces and maintain the desired true course, the ship's heading angle ψ deviates from α of an angle $\alpha' = \alpha - \psi$, leading to a different effective required thrust and a non-null rudder angle δ_R compared to the calm water case. To capture such behaviour, this study uses a 3-DoF quasi-dynamic model, focusing on the degrees of freedom associated with longitudinal drift force, transversal drift force, and yawing moment. In Fig. 4, conventions for angles and speeds are defined. All absolute angles are measured from the North direction and are considered positive in the clockwise direction.

All angles referred to the ship's heading (denoted by $'$) are measured from the direction of the ship's bow and are considered positive in the clockwise direction. Furthermore, the ship-fixed reference system $OXYZ$ used to measure forces and moments is defined in Fig. 4. This system is utilized to formulate the equilibrium equations of the ship, with its origin positioned at the midship section, having the X-axis facing stern to bow, the Y-axis facing port to starboard, and the Z-axis facing down (yawing moments are positive clockwise). It is noteworthy that, according to this convention, the advance speed $V = V_l \cdot \cos\alpha'$ is the component of ship speed V_l along the X-axis. However, the actual longitudinal and transverse speed components, u_{r_c} and v_{r_c}, relative to the ship must be calculated considering current speed and direction as defined in Appendix A.

3.3.1. System of equations

Given a subleg, the equilibrium of all the forces acting on the ship can be expressed in the ship-fixed reference system. Given that the required speed over the ground and true course is known (as defined in the itinerary), the unknowns in the system include the heading of the ship ψ, the rudder angle δ_R, and the effective longitudinal force exerted by the propeller, denoted as R_T. This force is devoted to counterbalancing all the longitudinal components of other forces. The symbol R_T is chosen, as it is commonly used to define the effective

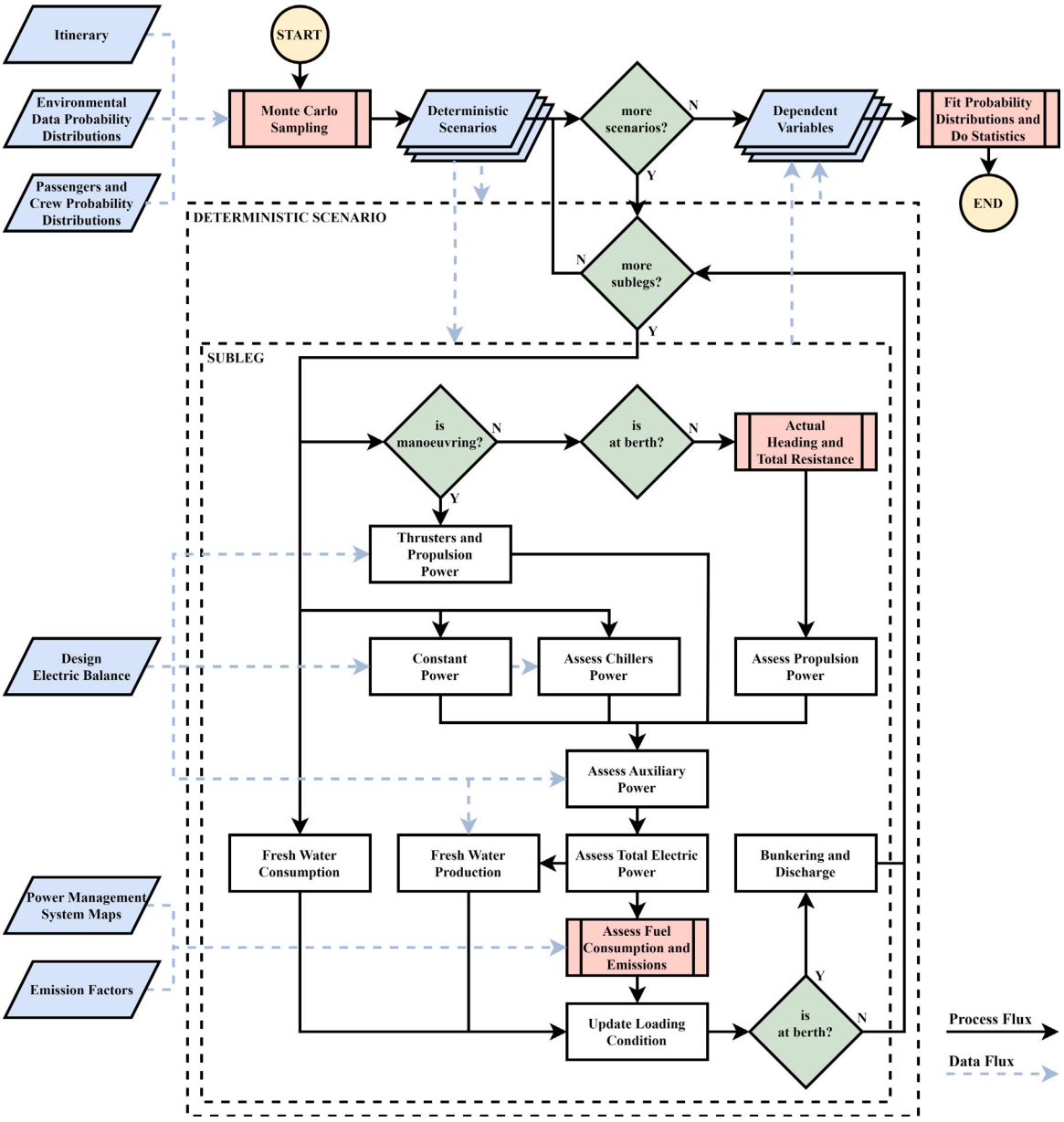

Fig. 3. Flowchart of the proposed probabilistic simulation process.

power of the ship ($P_E = R_T \cdot V = T \cdot (1-t)$) where T is the propeller thrust and t the thrust deduction factor, representing the power required to sustain the ship's advance speed V.

For the 3-DoF model, the equilibrium equations are as follows:

$$\begin{cases} 0 = R_T + X_{hydro}(\psi) + X_{wind}(\psi) + X_{wave}(\psi) + X_{rud}(\psi, R_T, \delta_R) \\ 0 = Y_{hydro}(\psi) + Y_{wind}(\psi) + Y_{wave}(\psi) + Y_{rud}(\psi, R_T, \delta_R) \\ 0 = M_{hydro}(\psi) + M_{wind}(\psi) + M_{rud}(\psi, R_T, \delta_R) \end{cases} \tag{4}$$

where X, Y, and M denote the longitudinal forces, transversal forces, and yawing moments, respectively, in the ship-fixed reference system. The subscript *hydro* denotes the hydrodynamic forces and moments originating from the interaction between the hull and fluid in calm water (in particular, X_{hydro} is the hull base resistance corrected to account for active stabilizers, fouling, loading condition and shallow water), *wind* represents those related to the wind, *wave* corresponds to those associated with the actual sea state (in particular, X_{wave} is commonly defined as added resistance in waves), and *rud* accounts for the forces generated by the rudder. The system is nonlinear in the variables $\mathbf{x} = (\psi, R_T, \delta_R)$. Consequently, it is solved here using a trust-region dogleg algorithm (Powell, 1968; Moré et al., 1980), which is grounded in the interior-reflective Newton method while employing a subspace trust-region approach, as detailed in Coleman and Li (1996) and Coleman and Li (1994). During each iteration, the algorithm approximates the solution to a large linear system by utilizing the preconditioned conjugate gradients method. The tolerance on the solution has been set to 0.001 N and 0.001 Nm for forces and moments, respectively while the following initial condition is adopted:

$$\mathbf{x}_0 = (\alpha, X_{hydro}(\alpha) + X_{wind}(\alpha) + X_{wave}(\alpha), 0) \tag{5}$$

This setup reflects a scenario where the ship maintains identical true course and heading angles ($\alpha' = 0$).

3.3.2. Correction of base resistance curve

The resistance curve in calm water, accounting for the effect of fixed appendages, denoted as $R_b(u_{r_c})$ (where u_{r_c} is the longitudinal component of relative current speed defined as for Appendix A), is typically determined through various means, including full-scale measurements, towing tank tests, empirical methods, or computational fluid

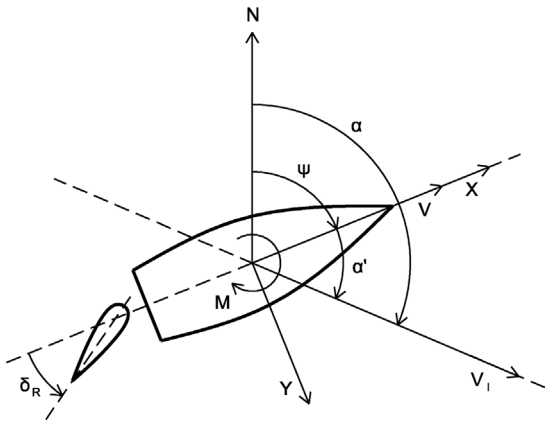

Fig. 4. Ship fixed reference system and conventions for angles and speeds.

dynamics. However, it is usually associated with the design draught T_{des} and does not consider the actual loading condition, shallow water, retractable appendages, and hull fouling. Therefore, at the onset of each subleg, it is corrected to accommodate these factors, resulting in the corrected resistance $R_c(u_{r_c})$. This corrected resistance is then utilized in the computation of hydrodynamic forces.

Firstly, fouling leads to an increase in hull roughness and, consequently, resistance. The additional resistance due to fouling is assessed here using an empirical method to incorporate the increase in hull roughness (Kresic and Haskell, 1983). The method considers two components of hull roughness M_{aa}: a linear increase of 2.8 μ m/month while in port and a component related to biofouling accumulation, considered only after the end of the anti-fouling paint lifespan. It is assumed that the initial hull roughness (at launching) M_{aa_0} and the anti-fouling paint's lifespan are 100 μ m and 1 year, respectively. After dry-docks, the hull roughness is presumed to return to the initial value (Molland, 2008), while after hull polishing at sea, only the biofouling effect on hull roughness is removed. Moreover, since anti-fouling paint is not applied during at-sea hull polishing operations, biofouling accumulation begins immediately after polishing. Once M_{aa} is determined, the additional resistance due to fouling is calculated as Malone and Little (1980), Townsin and Byrne (1980):

$$R_{rough}(u_{r_c}) = \frac{1}{2}\rho_w S(dC_F(M_{aa}) - dC_F(M_{aa_0}))u_{r_c}^2 \tag{6}$$

where S is the hull wetted surface area and dC_F is defined as:

$$dC_F(M_{aa}) = 105\left[\left(\frac{M_{aa}\cdot 10^{-6}}{L_{WL}}\right)^{\frac{1}{3}} - 0.64\right]\cdot 10^{-3} \tag{7}$$

Next, the impact of active stabilizers is incorporated into the base resistance. Typically, cruise ships are equipped with active stabilizers, which are engaged in rough seas to diminish ship roll. This introduces an average additional resistance denoted as R_{fins}. In the model, this average force is considered only in sea states 5 or higher ($H_{1/3} \geq 2.5$ m) and is evaluated using the methodology proposed by Holtrop et al. (1982):

$$R_{fins}(u_{r_c}) = \frac{1}{2}\rho u_{r_c}^2 A_{fins}(1 + k_{fins})C_F(u_{r_c}) \tag{8}$$

Here, A_{fins} is the fins' wetted surface area, $(1 + k_{\text{fins}})$ the appendage resistance factor of the fins and C_F denotes the ship frictional resistance factor, computed using the ITTC-1957 formulation (ITTC, 1957).

Subsequently, the obtained resistance is adjusted to accommodate the loading condition. At the onset of each subleg, the ship's loading condition is updated by evaluating the filling factors of fuel, FW, and GBW tanks, as previously described. This adjustment induces changes in the ship's displacement and draught, thereby modifying the vessel's resistance. In the context of cruise ships, characterized by a short interval between maximum and minimum seagoing draughts, the resistance correction is also relatively modest. Nonetheless, it is accounted for here according to the Admiralty formula:

$$R_{fc}(u_{r_c}) = [R_b(u_{r_c}) + R_{rough}(u_{r_c}) + R_{fins}(u_{r_c})]\left(\frac{T}{T_{des}}\right)^{\frac{2}{3}}\frac{\rho_w}{1025} \tag{9}$$

where T and T_{des} are the actual and design draughts respectively.

Finally, the obtained resistance $R_{fc}(u_{r_c})$ is once again adjusted to account for the shallow water effect, resulting in the final $R_c(u_{r_c})$. In the context of the studied problem, which aims to define the probability distribution of emissions for the entire itinerary, the impact of shallow water is significant only when long sublegs at high speed are navigated in shallow water. Therefore, the most concerning condition is incipient shallow water, modelled here according to the empirical Lackenby formulation, as recommended by ITTC (ITTC, 2014; Lackenby, 1963). The method complements the classical Schlichting method with a similar approach. Given a reference speed, the effect of shallow water resistance is modelled by introducing a speed loss while keeping the resistance constant. In the Lackenby method, the non-dimensional speed loss factor $\Delta u_{r_c}/u_{r_c}$ due to incipient shallow water is given by:

$$\frac{\Delta u_{r_c}}{u_{r_c}} = 0.1242\left(\frac{A_M}{h^2} - 0.05\right) + 1 - \sqrt{\tanh\left(\frac{gh}{u_{r_c}^2}\right)} \tag{10}$$

where h is the water depth in m, A_M midship section area underwater in m^2 and u_{r_c} the open water ship speed in m/s.

3.3.3. Hull hydrodynamic forces

The hydrodynamic forces are calculated by considering the impact of the ship's speed and sea current. The longitudinal component is determined through interpolation on the corrected resistance curve R_c. In this interpolation, the current's longitudinal component of the relative speed u_{r_c} (see Appendix A) is considered as the actual speed:

$$X_{hydro}(\psi) = -R_c(u_{r_c}) = -R_c\left(V_{r_c}(\psi)\cos[\beta'_r(\psi)]\right) \tag{11}$$

where $V_{r_c}(\psi)$ and $\beta'_r(\psi)$ are the relative speed of the sea current and its angle from the heading, respectively. The transversal component of the hydrodynamic force and the yawing moment are evaluated according to Fossen (2011) as:

$$\begin{aligned} Y_{hydro}(\psi) &= \tfrac{1}{2}\rho_w A_D[V_{r_c}(\psi)]^2 C_{Y_h}(\psi) \\ M_{hydro}(\psi) &= \tfrac{1}{2}\rho_w A_D L_{OA}[V_{r_c}(\psi)]^2 C_{M_h}(\psi) \end{aligned} \tag{12}$$

where A_D is the lateral projected area underwater, considering the actual draught, L_{OA} is the overall length of the ship, and the coefficients $C_{Y_h}(\psi)$ and $C_{M_h}(\psi)$ are given by:

$$\begin{aligned} C_{Y_h}(\psi) &= C_{Y_h}^{max}\sin[\beta'_r(\psi)]|\sin[\beta'_r(\psi)]| \\ C_{M_h}(\psi) &= C_{M_h}^{max}\sin[2\beta'_r(\psi)] \end{aligned} \tag{13}$$

where $C_{Y_h}^{max}$ and $C_{Y_h}^{max}$ are their maximum values, which can be assumed as constants for different kinds of ships.

3.3.4. Wind forces

The wind forces are evaluated using Blendermann's method (Blendermann, 2014) considering the relative speed of the wind (see Appendix A). The forces are then assessed as:

$$\begin{aligned} X_{wind}(\psi) &= \tfrac{1}{2}\rho_a A_F[V_{r_w}(\psi)]^2 C_{X_w}(\psi) \\ Y_{wind}(\psi) &= \tfrac{1}{2}\rho_a A_L[V_{r_w}(\psi)]^2 C_{Y_w}(\psi) \\ M_{wind}(\psi) &= \tfrac{1}{2}\rho_a A_L L_{OA}[V_{r_w}(\psi)]^2 C_{M_w}(\psi) \end{aligned} \tag{14}$$

where ρ_a is the air density, A_F and A_L are the frontal and lateral projected areas of the ship above the waterline, considering the actual draught, $V_{r_w}(\psi)$ is the relative speed of the wind (apparent wind),

and $C_{X_w}(\psi)$, $C_{Y_w}(\psi)$, and $C_{M_w}(\psi)$ are the Blendermann's coefficients defined as:

$$\begin{aligned} C_{X_w}(\psi) &= -CD_l \frac{A_L}{A_F} \frac{\cos[\gamma_r'(\psi)]}{1-\frac{\delta}{2}\left(1-\frac{CD_l}{CD_t}\right)\sin^2[\gamma_r'(\psi)]} \\ C_{Y_w}(\psi) &= CD_t \frac{\sin[\gamma_r'(\psi)]}{1-\frac{\delta}{2}\left(1-\frac{CD_l}{CD_t}\right)\sin^2[\gamma_r'(\psi)]} \\ C_{M_w}(\psi) &= \left[\frac{s_L}{L_{OA}} - 0.18\left(|\gamma_r'(\psi)| - \frac{\pi}{2}\right)\right] CY_w \end{aligned} \tag{15}$$

where $\gamma_r'(\psi)$ is the angle between the heading and relative speed of the wind, s_L is the distance of the centroid of lateral project area from the origin of ship-fixed reference system, whereas CD_l, CD_t, and δ are constants defined according to the kind of ship.

3.3.5. Wave forces

Wave forces are decomposed into two components: added resistance in waves X_{wave} and transversal drift force Y_{wave}. The added resistance in regular waves $R_{AW}/\zeta^2(\omega_e, \psi)$ has been assessed according to a statistical method (Liu and Papanikolaou, 2020) accounting for diffraction effects (Faltinsen, 1980) and introducing semi-empirical parameters to approximate the added resistance under different wave headings. The drift force in regular waves $F_Y/\zeta^2(\omega_e, \psi)$ has been assessed with another statistical method (Jinkine and Ferdinande, 1974) having similar features. Both forces in regular waves are computed as a function of encounter frequency ω_e, actual heading angle $\chi = \psi - \delta$, and thus, are derived as a function of the angle ψ. These empirical methods have been chosen here since they are the only ones available in the literature that have been developed and tested also for cruise ships.

Given the $H_{1/3}$ and T_z identifying the sea state in a subleg, the sea spectrum is defined according to the Pierson–Moskowitz formulation (Moskowitz et al., 1962-63) expressed as a function of wave frequency ω as:

$$S_\zeta(\omega) = \frac{Ag^2}{\omega^5} \exp\left[-B\left(\frac{g}{\omega}\right)^4\right] \tag{16}$$

where:

$$\begin{aligned} A &= 4\pi^3 \left(\frac{H_{1/3}}{gT_z^2}\right)^2 \\ B &= \frac{16\pi^3}{(gT_z)^4} \end{aligned} \tag{17}$$

which can be written as a function of ω_e as :

$$S_\zeta(\omega_e) = S_\zeta(\omega) \frac{g}{g - 2\omega V_l \cos(\psi - \delta)} \tag{18}$$

Then, wave forces are evaluated as Faltinsen (1980), Lang and Mao (2020):

$$\begin{aligned} X_{wave}(\psi) &= -2\int_0^\infty \frac{R_{AW}}{\zeta^2}(\omega_e, \psi) S_\zeta(\omega_e) d\omega_e \\ Y_{wave}(\psi) &= 2\int_0^\infty \frac{F_Y}{\zeta^2}(\omega_e, \psi) S_\zeta(\omega_e) d\omega_e \end{aligned} \tag{19}$$

3.3.6. Rudder forces

The hydrodynamic forces exerted by the rudder are evaluated as follows:

$$\begin{aligned} X_{rud}(\psi, R_T, \delta_R) &= -L(\psi, R_T, \delta_R)\sin[\delta_R - \delta_e(\psi, R_T, \delta_R)] \\ &\quad - D(\psi, R_T, \delta_R)\cos[\delta_R - \delta_e(\psi, R_T, \delta_R)] \\ Y_{rud}(\psi, R_T, \delta_R) &= -L(\psi, R_T, \delta_R)\cos[\delta_R - \delta_e(\psi, R_T, \delta_R)] \\ &\quad + D(\psi, R_T, \delta_R)\sin[\delta_R - \delta_e(\psi, R_T, \delta_R)] \\ M_{rud}(\psi, R_T, \delta_R) &= -X_R Y_{rud}(\psi, R_T, \delta_R) \end{aligned} \tag{20}$$

where the attack angle δ_e, the lift force L and drag force D are defined as:

$$\begin{aligned} \delta_e(\psi, R_T, \delta_R) &= \delta_R + \text{atan2}[v_R(\psi, R_T), u_R(\psi, R_T)] \\ L(\psi, R_T, \delta_R) &= n_S \tfrac{1}{2}\rho_w A_R [V_R(\psi, R_T)]^2 C_L(\psi, \delta_R) \\ D(\psi, R_T, \delta_R) &= n_S \tfrac{1}{2}\rho_w A_R [V_R(\psi, R_T)]^2 C_D(\psi, \delta_R) \end{aligned} \tag{21}$$

where n_S is the number of propellers/rudders (cruise ships are usually twin-screw, hence $n_S = 2$), A_R is the longitudinal projected area of the rudder, X_R is the longitudinal coordinate of the A_R centre in the ship-fixed reference system, $V_R(\psi, R_T) = (u_R, v_R)$ is the speed of the incident flow on the rudder, whereas $C_D(\delta_R)$ and $C_L(\delta_R)$ are the drag and lift coefficients of the rudder, respectively. Since the rudder is used only to maintain the true course (small rudder angles), and there is no interest in investigating ship manoeuvring, the lift coefficient has been evaluated using a linear derivative:

$$C_L(\psi, \delta_R) = \frac{\partial C_L}{\partial \delta_e}\delta_e(\psi, R_T, \delta_R) \tag{22}$$

where, according to Molland and Turnock (2011), the derivative is estimated as:

$$\frac{\partial C_L}{\partial \delta_e} = 1.95\pi \frac{\lambda}{\lambda + 3} \tag{23}$$

with λ as the elongation ratio of the rudder. Concerning the drag coefficient, it shall consider only the increase in rudder resistance due to the rudder angle, as the null-angle resistance is already included in the calm water resistance. Thus, it is evaluated as a function of the generated lift (Molland and Turnock, 2011):

$$C_D(\psi, \delta_R) = \frac{[C_L(\psi, \delta_R)]^2}{0.86\pi\lambda} \tag{24}$$

The evaluation of flow speed on the rudder is carried out considering both the hull effect and the flow acceleration induced by the propeller. The advance speed V_A and propeller thrust T are evaluated as:

$$\begin{aligned} V_A(\psi) &= u_{r_c}(\psi)[1 - w(\psi)] \\ T(\psi, R_T) &= \frac{R_T}{n_S[1-t(\psi)]} \end{aligned} \tag{25}$$

where $V_{r_c}(\psi) = (u_{r_c}, v_{r_c})$ is the relative speed of the current (see Appendix A), $w(\psi)$ and $t(\psi)$ are the wake fraction and the thrust deduction factor, both expressed as a function of ship speed and here evaluated by interpolation assuming the vessel speed $u_{r_c}(\psi)$. Then, the components of the rudder incident flow speed are estimated as:

$$\begin{aligned} u_R(\psi, R_T) &= V_A(\psi)\frac{1+\sqrt{1+C_T(\psi, R_T)}}{2} \\ v_R(\psi) &= v_{r_c}(\psi) \end{aligned} \tag{26}$$

where $C_T(\psi, R_T)$ is the thrust loading coefficient of the propeller given by:

$$C_T(\psi, R_T) = \frac{T(\psi, R_T)}{\frac{1}{2}\rho_w A_0 [V_A(\psi)]^2} \tag{27}$$

3.4. Tank-to-wake emission assessment

In this study, emissions arising from fuel combustion in diesel engines are taken into account, i.e. Tank-to-Wake (TtW) emissions. To assess these emissions, the cruise ship's electric power demand must first be calculated. Subsequently, through an appropriate mapping operation to model the Power Management System (PMS), the electric power demand is converted into fuel consumption, leading to the estimation of the corresponding equivalent tons of carbon dioxide (CO_2) emitted. Additionally, statutory indicators can be forecasted for the considered itinerary.

3.4.1. Electric power demand

Once System (4) is solved, using Eq. (25), the advance speed V_A and propeller thrust T can also be calculated. Subsequently, they can be used to evaluate the Papmel coefficient:

$$\left(\frac{K_T}{J^2}\right)^* = \frac{T}{\rho_w V_A^2 D_p^2} \tag{28}$$

where K_T is the thrust coefficient of the propeller, J is its advance coefficient, and D_p is its diameter. The propeller curves providing the

thrust and torque coefficients as functions of J ($K_T(J)$ and $K_Q(J)$, respectively), are firstly corrected to account for fouling, as described in Kresic and Haskell (1983). Then, the propeller functioning point J^* is found by interpolation on the curve $J(K_T/J^2)$ corresponding to the value $\left(K_T/J^2\right)^*$. Then, the absorbed torque Q and revolutions per second (rps) n_p of the propeller are defined by:

$$\begin{aligned} Q &= K_Q(J^*)\rho_w n_p^2 D_p^5 \\ n &= \frac{V_A}{J^* D_p} \end{aligned} \tag{29}$$

Thus, the brake power provided by the PEM is:

$$P_B = \frac{2\pi n_p Q}{\eta_r \eta_s} \tag{30}$$

where η_r and η_s are the relative rotative and shaft efficiency, respectively.

If P_B exceeds the maximum power of the PEM P_B^{max} or n_p exceeds the maximum speed of the PEM, the condition that solves System (4) cannot be sustained, and the ship will be not capable to reach the speed V_l on the analysed subleg. Hence, the scheduled arrival time is disrupted and the ship will arrive delayed at the end of the subleg. In such a case, P_B is assumed to be equal to P_B^{max}, and the subleg is flagged as "delayed" in the deterministic scenario under analysis. By dividing the number of "delayed" scenarios by the total number of scenarios, the risk of itinerary disruption due to environmental factors can be assessed.

Following the assessment of P_B, the propulsion electric power P_{prop} provided by the ship's main switchboards is given by:

$$P_{prop} = \frac{n_S P_B}{\eta_{PEM}\left(\frac{P_B}{P_B^{max}}\right)\eta_{tc}} \tag{31}$$

where $\eta_{PEM}(P_B/P_B^{max})$ is the PEM efficiency expressed as a function of its load, and η_{tc} is the efficiency of electric transformers and converters. Finally, the electric power demand to the onboard power plant P_{el} is calculated as:

$$\begin{aligned} P_{noaux} &= P_{prop} + P_{ch}(T_a) + P_{fw} + P_{scrub} + P_{const} \\ P_{el} &= \frac{P_{noaux} + P_{aux}(P_{noaux})}{\eta_{sw}} \end{aligned} \tag{32}$$

where η_{sw} represents the efficiency of switchboards and the distribution system.

3.4.2. Standard power management system

On a cruise ship, as with all diesel–electric vessels, electric power is supplied by multiple diesel generators. The number and load of active generators are regulated by the PMS or manually adjusted by engineer officers (Vasilikis et al., 2022). Current PMSs typically employ straightforward rules based on the load l_g of the generators, defined as:

$$l_{g_i} = \frac{P_{el_i}}{\eta_G P_i^{max}} \tag{33}$$

where P_{el_i} is the actual electric power produced by the generator, P_i^{max} is the engine's maximum continuous rating, and η_G is the generator efficiency. The basic rules of a standard Power Management System (PMS) can be summarized as follows:

- All active diesel generators operate with an equal load l_g.
- If l_g exceeds an upper threshold (typically 0.85) for a specified time interval, an additional generator is automatically activated.
- If l_g falls below a lower threshold (typically 0.20) for a specified time interval, a generator is automatically deactivated.

In practice, generators often come in two different sizes, forming a father–son configuration, which complicates the PMS rules. Moreover, some ships may have generators using different types of fuel. For instance, if only certain generators are equipped with an exhaust gas system including scrubbers, they can use HSFO, while others are compelled to use more expensive fuels like VLSFO or MGO. Consequently, additional rules or manual interventions might be implemented to preferentially use generators fuelled with HSFO.

In the simulation process, these rules are represented through a mapping procedure that determines the fuel consumption fc_j in t/h for each jth type of fuel as a function of the power P_{el} required by the power plant, as given by Eq. (32). Especially in the case of a father–son power plant, there can be multiple viable configurations of active engines. A configuration is deemed viable if the sum of the electric power of all n_a active generators equals P_{el}, and the global load l_g falls within the lower and upper thresholds. The global load of the power plant is defined as:

$$l_g = l_{g_1} = \cdots = l_{g_{n_a}} = \frac{P_{el}}{P_G} \tag{34}$$

where P_G is the maximum electric power provided by diesel generators and defined as:

$$P_G = \eta_G \sum_i^{n_a} P_i^{max} \tag{35}$$

For the kth configuration, the fuel consumption in t/h of the jth type of fuel can be evaluated as:

$$fc_{jk} = \sum_i^{n_{jk}} d_j SFOC_{ij}(l_{g_i}) P_i^{max} l_{g_i} \cdot 10^{-6} \tag{36}$$

where n_{jk} denotes the number of active generators utilizing the jth fuel, d_j represents a coefficient accounting for depuration/filtering allowance (assumed to be 1.015 for HSFO and VLSFO, and 1 for MGO), and $SFOC_{ij}(l_{g_i})$ represents the specific fuel consumption in g/kWh of the ith engine at load l_{g_i}. Considering all the viable configurations of the power plant, the fuel consumption map is given by:

$$fc(P_{el}) = \min_k \sum_j^{n_f} fc_{jk} \tag{37}$$

where n_f is the number of fuel types used. This means that, among the viable configurations, the one minimizing the overall fuel consumption is chosen.

3.4.3. Optimized power management system

An optimized PMS is capable of further reducing fuel consumption and emissions compared to standard ones (Kanellos, 2014). To model an optimized PMS, a specific map $fc_o(P_{el})$ needs to be developed. The adopted methodology is the same as the standard one (according to Eq. (36),(37)), except for the assessment of the fuel consumption of each viable configuration.

For a given kth viable configuration and a required power P_{el}, the fuel consumption is determined by solving an optimization problem, where the loads of active generators are chosen individually to meet P_{el} at the minimum emissions cost. This optimization problem is formulated as:

$$\begin{cases} \text{find} & \mathbf{x} \\ \text{minimize} & f(\mathbf{x}) \\ \text{subject to} & \begin{cases} \mathbf{h}(\mathbf{x}) = 0 \\ \mathbf{g}_{max}(\mathbf{x}) \le 0 \\ \mathbf{g}_{min}(\mathbf{x}) \le 0 \end{cases} \end{cases} \tag{38}$$

where the variables are the loads of each generator:

$$\mathbf{x} = (l_{g_1}, \ldots, l_{g_{n_a}}) \tag{39}$$

The objective function is defined as:

$$f(\mathbf{x}) = \sum_j^{n_f} \sum_i^{n_j} EF_j SFOC_{ij}(x_i) P_i^{max} x_i \tag{40}$$

Table 3
Assumed Tank-to-Wake emission factors for internal combustion engines (IMO, 2023a).

Fuel type	EF
	(gCO_2e/gFuel)
HSFO	3.114
VLSFO	3.114
MGO	3.206

where EF_j represents the emission factor for the jth type of fuel used. To ensure that the n_k active engines generate the required power, the equality constraints are defined as:

$$\mathbf{h}(\mathbf{x}) = P_{el} - \sum_{i}^{n_k} P_i^{max} x_i \tag{41}$$

To maintain all engines within an acceptable load range $[l_{\min}, l_{\max}]$, the inequality constraints are defined as:

$$\begin{aligned} \mathbf{g}_{max}(\mathbf{x}) &= \mathbf{I} \times \mathbf{x} - l_{max} \\ \mathbf{g}_{min}(\mathbf{x}) &= -\mathbf{I} \times \mathbf{x} + l_{min} \end{aligned} \tag{42}$$

where $\mathbf{I}$ is the identity matrix.

To solve the optimization problem, the interior-point algorithm is employed (Byrd et al., 1999, 2000; Waltz et al., 2006; Nocedal et al., 2014). The initial condition is assumed to have an equal distribution of load, as in Eq. (34).

$$\mathbf{x}_0 = (l_g, \ldots, l_g) \tag{43}$$

3.4.4. Statutory emission factors and indicators

Given the fuel consumption for each fuel type utilized in the standard or optimal configuration, the corresponding emissions of equivalent tons of CO_2 for the analysed subleg are determined as:

$$CO_2e_l = \sum_{j}^{n_f} EF_j fc_j \frac{d_l}{V_l} \tag{44}$$

where d_l is the distance covered by the ship in the subleg and V_l its speed, both related to true route.

Thus, the total emissions (CO_2e) can be calculated by summing the contributions from all sublegs of the itinerary. The emission factors used are sourced from IMO (2023a) and are detailed in Table 3. In the present work, Tank-to-Wake emissions have been considered solely in accordance with currently enforced guidelines for operational index assessment (IMO, 2022, 2018).

The emissions can be utilized to calculate the statutory indicators for the ship's environmental performance over the entire itinerary. In this context, the Carbon Intensity indicator (CII) is employed, although its efficacy has recently been questioned, and alternative formulations for cruise ships have been suggested (Braidotti et al., 2023). According to the currently applicable regulations (IMO, 2021b), the attained CII for a cruise vessel, concerning a specific itinerary, can be defined as:

$$CII = \frac{CO_2e}{GT \cdot d} \tag{45}$$

where GT represents the gross tonnage of the ship, and d denotes the total distance covered in the itinerary (the sum of all d_l). The attained value is to be compared to a required value, which declines over the years according to IMO (2021a). Finally, based on its attained value and the corresponding year, the ship is assigned a grade ranging from A (best emissions ranking) to E (worst emissions ranking) as per (IMO, 2021c).

In this analysis, other mandatory indicators not strictly tied to operational conditions, such as EEXI, are omitted as they are not contingent on the actual emissions (CO_2e).

Table 4
Main particulars of Test Ship.

Dimension	ID	Value	Unit
Length between perpendicular	L_{BP}	290	m
Length overall	L_{OA}	323	m
Design beam	B	41	m
Design draft	T	8.55	m
Gross Tonnage	GT	153 000	GT
Number of propellers		2	
Propeller diameter	D	6.1	m
Number of blades	Z	6	
Pitch-Diameter Ratio	P/D	1.073	
Expanded Area Ratio	A_E/A_0	0.782	
Number of Generators		4	
Installed power	P_{tot}	62 400	kW
Propulsion Electric Motors Power	P_{PEM}	2 × 21000	kW
Evaporator nominal production rate		2 × 30	t/h
Reverse osmosis nominal production rate		2 × 30	t/h
Maximum Passengers number		5179	
Maximum Crew members number		1532	
HSFO tanks capacity		1960	m^3
VLSFO tanks capacity		1540	m^3
MGO tanks capacity		1216	m^3
FW tanks capacity		4341	m^3

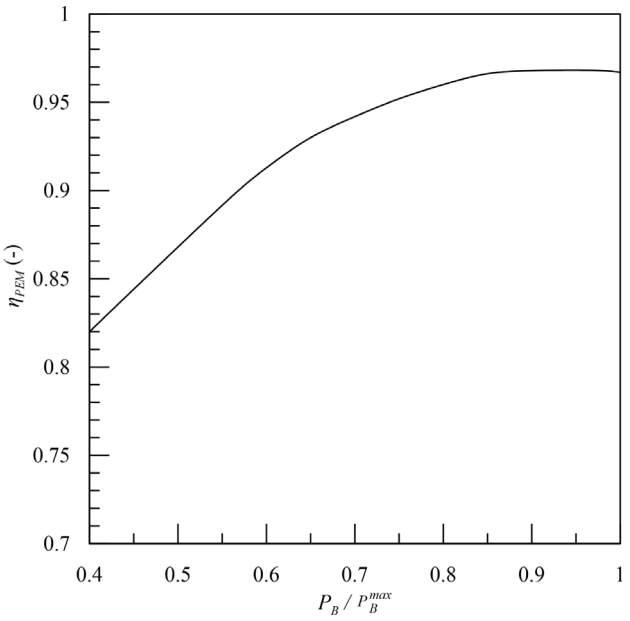

Fig. 5. PEM efficiency as a function of PEM load.

4. Test ship

An existing ship from a prominent cruise company has been chosen as a test case, with its main particulars reported in Table 4.

4.1. Propulsion system

The propulsion system of the test ship is diesel–electric. The propulsion of the ship is assured by 2 Propulsion Electric Motors (PEM) having a maximum power of 21 MW each and efficiency as a function of the engine load according to Fig. 5. The conventional shaft line connecting the PEM and the propeller has an efficiency η_s of 0.970. The calm water resistance is provided in Fig. 6, whereas the propeller open water diagram is given in Fig. 7.

4.2. Electric generation and distribution system

The onboard power plant comprises four diesel generators arranged in a father–son configuration, as outlined in Table 5. The generators

Table 5
Characteristics of the test ship's electric generators (Wärtsilä, 2024).

ID	Model	Type	Fuel	Location	Scrubber	P^{min} (kW)	P^{max} (kW)	η_G (–)
1	Wärtsilä 12V46F	Diesel Genset	MGO/HSFO/VLSFO	Fore Engine Room	Yes	2880	14400	0.97
2	Wärtsilä 12V46F	Diesel Genset	MGO/HSFO/VLSFO	Aft Engine Room	No	2880	14400	0.97
3	Wärtsilä 16V46F	Diesel Genset	MGO/HSFO/VLSFO	Fore Engine Room	Yes	3360	16800	0.97
4	Wärtsilä 16V46F	Diesel Genset	MGO/HSFO/VLSFO	Aft Engine Room	No	3360	16800	0.97

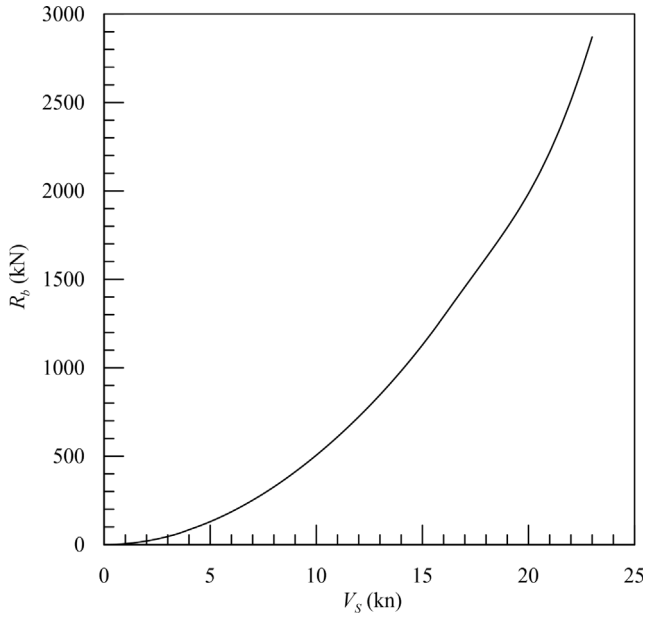

Fig. 6. Test ship's calm water resistance.

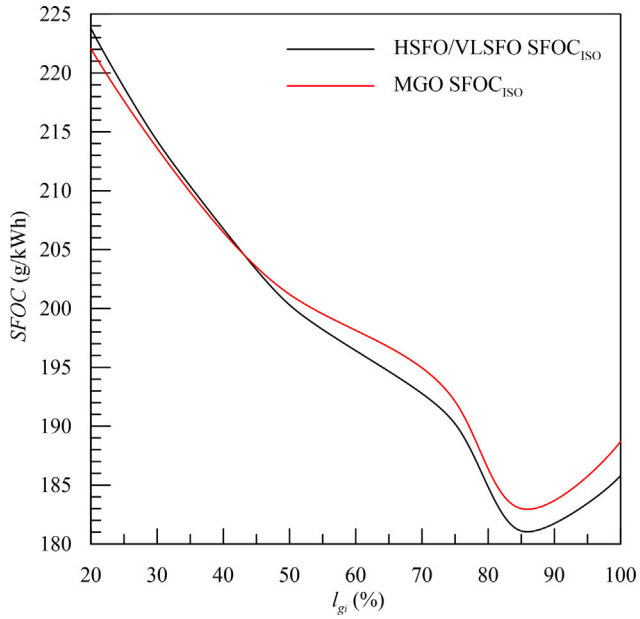

Fig. 8. $SFOC_{ISO}$ as a function of engine load.

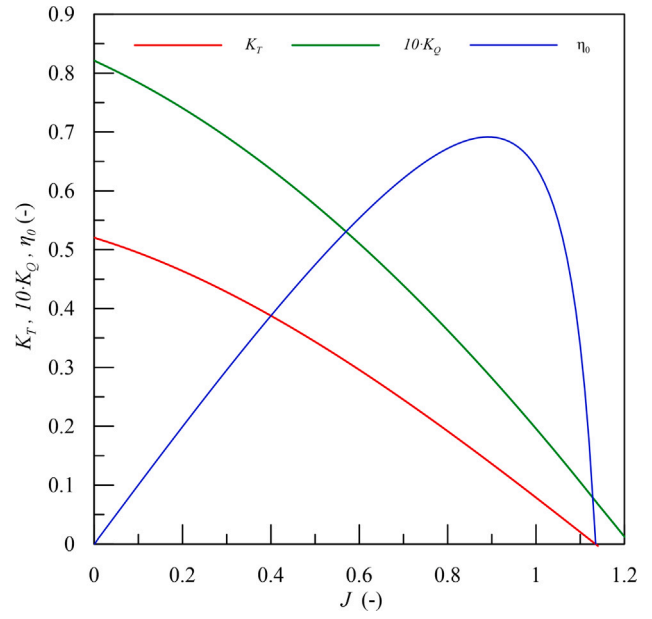

Fig. 7. Open water propeller diagram without fouling.

have the $SFOC$ characteristics as depicted in Fig. 8, considering ISO conditions (ISO Ships, 2015). Notably, the two generators located in the fore engine room, specifically one father and one son unit, are equipped with scrubbers. Thus, under normal conditions, HSFO is used as fuel due to its lower cost, while scrubbers can remove Sulphur oxides (SO_x). If the engines are equipped with scrubbers, HSFO can be used for navigation within a Sulphur Emission Control Area and in ports as well, except for French ports where MGO must be used due to national regulations. In contrast, the two generators situated in the aft engine room are required to utilize VLSFO or MGO to comply with environmental regulations regarding SO_x emissions. MGO is typically used at berth, during manoeuvres, within the first 3 nm before arrival at port, and after departure. Regarding the electric distribution system, the switchboard efficiency (η_{sb}) is 0.999, while the efficiency of the propulsion transformers and converters (η_{tc}) is 0.975.

4.3. FW production, auxiliaries and chillers power demand

The ship is equipped with 2 reverse osmosis machines having a nominal production rate of 30 t/h and 2 evaporators having a nominal production of 30 t/h. Hence the maximum nominal production rate of the ship p_{FW}^{max} is equal to 120 t/h. The actual production of evaporators as a function of power plant load is given in Fig. 9. Fig. 10 provides the electric power demand related to auxiliaries. The installed auxiliary power P_{aux}^{max} is equal to 4037.2 kW. Fig. 11 provides the electric power demand from chillers as a function of external temperature. The chiller installed power P_{ch}^{max} is equal to 5037.1 kW. Finally, the constant power P_{const} for the test ship is equal to 5016.5 kW.

5. Test itineraries set-up

In this section, the test itineraries are presented as along with the environmental data sources and the fouling modelling assumptions. They are all derived from an existing itinerary, which is used to validate the deterministic simulation model with experimental data from past voyages. All the itineraries are then used to simulate the itinerary planning considering environmental data statistics to demonstrate the potential of proposed technique.

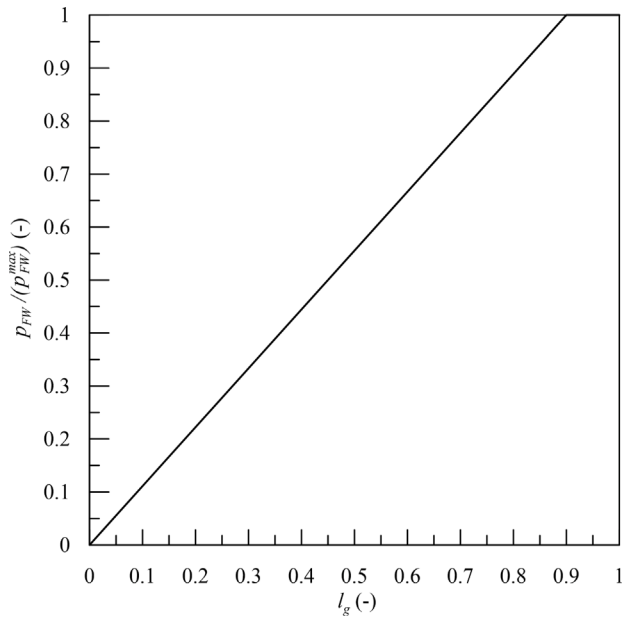

Fig. 9. Evaporators FW production on nominal FW production as a function of power plant load.

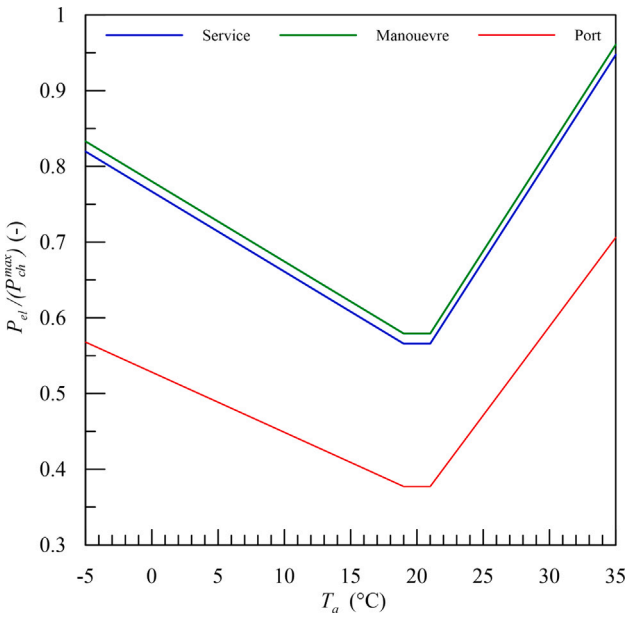

Fig. 11. Chillers electric power demand as a function of air temperature.

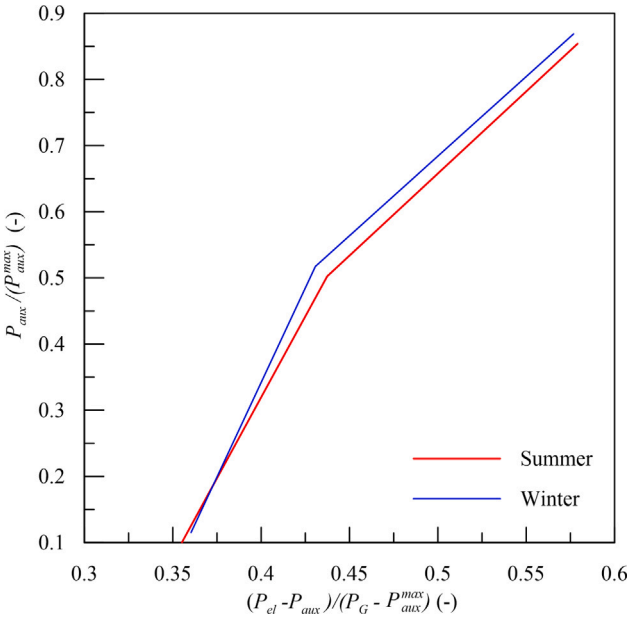

Fig. 10. Auxiliaries electric power demand as a function of the reminder of electric power demand.

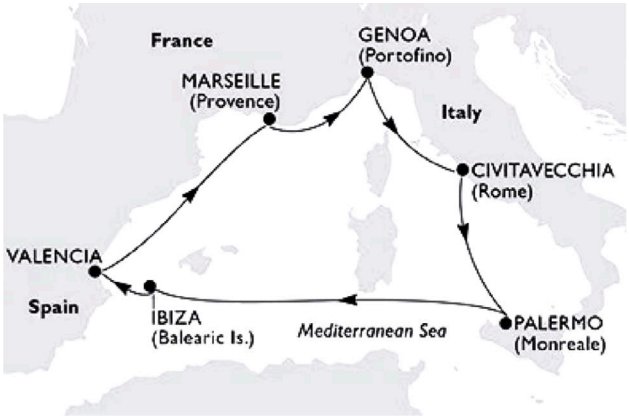

Fig. 12. Original West-Med existing itinerary.

5.1. Itineraries

In this study, five one-week cruise itineraries are simulated and compared. These itineraries are derived from a typical West-Mediterranean itinerary (see Fig. 12) with ports of call in Genoa (GOA), Civitavecchia (CVV), Palermo (PMO), Ibiza (IBZ), Valencia (VLC), Marseille (MRS), and concluding with a return to Genoa (GOA). The detailed itinerary is provided in Appendix B.

The following itineraries have been considered, with the symbol $*$ denoting reversed itineraries:

- Itinerary I:
  - Sequence: Original (GOA – CVV – PMO – IBZ – VLC – MRS - GOA)
  - Evaporators: active during navigation (production as per Fig. 9)
  - Reverse osmosis: active during navigation (constant production of 48 m^3/h)
  - PMS configuration: standard
- Itinerary II*:
  - Sequence: Reverse (GOA – MRS – VLC – IBZ – PMO – CVV – GOA)
  - Evaporators: active during navigation (production as per Fig. 9)
  - Reverse osmosis: active during navigation (constant production of 48 m^3/h)
  - PMS configuration: standard
- Itinerary III:
  - Sequence: Original (GOA – CVV – PMO – IBZ – VLC – MRS - GOA)
  - Evaporators: switched off

  - Reverse osmosis: switched off
  - PMS configuration: standard

- Itinerary IV*:
  - Sequence: Reverse (GOA – MRS – VLC – IBZ – PMO – CVV – GOA)
  - Evaporators: switched off
  - Reverse osmosis: switched off
  - PMS configuration: standard

- Itinerary IV^*_{Opti}:
  - Sequence: Reverse (GOA – MRS – VLC – IBZ – PMO – CVV – GOA)
  - Evaporators: switched off
  - Reverse osmosis: switched off
  - PMS configuration: optimized

5.2. Environmental conditions in west-med

Statistics on wave direction, significant wave height and zero-crossing periods were extracted from Hogben et al. (1986) during the summer months (June to August) in the Western Mediterranean Sea (Area 26). Based on these data, wind conditions are defined according to Fig. 2. Monthly average currents were extracted from North Atlantic pilot charts, which cover the Mediterranean Sea, for the respective month under analysis (NGIA, 2024). The monthly pdf for air temperature was established based on a decade of statistical data from a meteorological station located at Cape Caccia, Sardinia (TuTiempo, 2024). The station is centrally located within the considered area, hence it is considered representative of the area with a similar spacial resolution of wave data. Besides, while it may not provide precise data for every specific location, it is noteworthy that air temperature primarily influences the power demand of chillers, which is assessed using a simplified model derived from electric balance data. Therefore, for this initial work aimed at demonstrating the technique's potential, the selected air temperature data has been deemed sufficient.

5.3. Fouling condition

The ship used in simulations was inactive for approximately 6 months due to the COVID-19 pandemic. It underwent its first dry-dock at the end of June 2022, four years after its launching, without any propeller or hull cleaning during this period. This atypical service history resulted in severe fouling conditions, which have been modelled based on the following assumptions:

- Time since launching: 4 years
- Time spent at berth: 200 days/year (accounting for the COVID-19 inactivity)
- Effective life of antifouling paint: 1 year
- Bio-fouling coefficient severe (Kresic and Haskell, 1983): 1,052 μm/day
- Initial hull roughness: 100 μm
- Initial propeller roughness: 20 μm

After dry-dock, the duration of time spent at berth was reduced to 120 days per year, aligning with the typical operational schedule of the ship without prolonged stops. Furthermore, adjustments were made to account for the actual duration since dry-dock, incorporating corrections for hull and propeller fouling. The simulations of the test itineraries were conducted in July 2024, considering hull cleaning performed on June 6, 2023, and propeller polishing undertaken on June 22, 2023.

6. Results

This section presents the outcomes of the study. First, maps for the onboard PMS are shown in both standard and optimized versions. Subsequently, the model is validated using real data obtained before and after a dry-dock. Finally, the simulation results for the five aforementioned itineraries are presented.

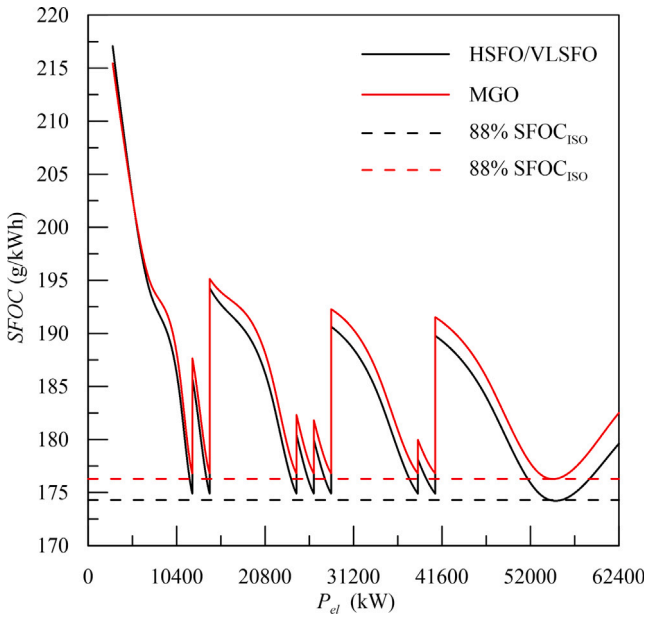

Fig. 13. Onboard power plant SFOC as a function of total required mechanical power in Standard PMS configuration.

6.1. PMS maps

Firstly, the resulting PMS maps are provided, as they are utilized in both the deterministic validation and probabilistic simulation processes. Figs. 13 and 14 present the SFOC maps in HSFO/VLSFO and MGO modes for standard and optimized PMS, respectively. For each value of mechanical power required from thermal engines, the corresponding SFOC of the power plant has been computed, taking into account all active thermal engines. Figs. 15 and 16 highlight the load of each thermal engine in standard and optimized PMS configurations, respectively. It is worth noting that, in the standard configuration, the lower and upper load limits has been set to 20% and 85%, respectively, following the configuration of a real ship's PMS. In the optimized configuration, the upper limit has been slightly increased to 88% to ensure that the engines can operate to their maximum efficiency point.

At low power plant loads, only one son engine is used, and the SFOC follows the trend shown in Fig. 8. As power demand increases above 88% of the maximum continuous rating, a switch to a different configuration of the power plant (set of active engines) is required. In the standard PMS, when the power demand calls for a switch, all the generators operate at low load. Conversely, the optimization process calls for only one son generator working off-design at low loads, while keeping all the other active generators at a relatively high load. Among them, if the other son generator is active, it works very close to the optimal load, while any other active father generator operates at a slightly lower load (about 75%). As the power demand increases, the load is mostly increased on the son engine working off-design only until it reaches the optimal load (the same as the other son engine, if active). This configuration has the effect of cutting down the peaks on the SFOC diagram that correspond to all generators working at low load in the standard configuration. Hence, using the optimized PMS, the overall power plant SFOC is kept well below 185 g/kWh instead of reaching values up to 195 g/kWh, as observed with the standard PMS.

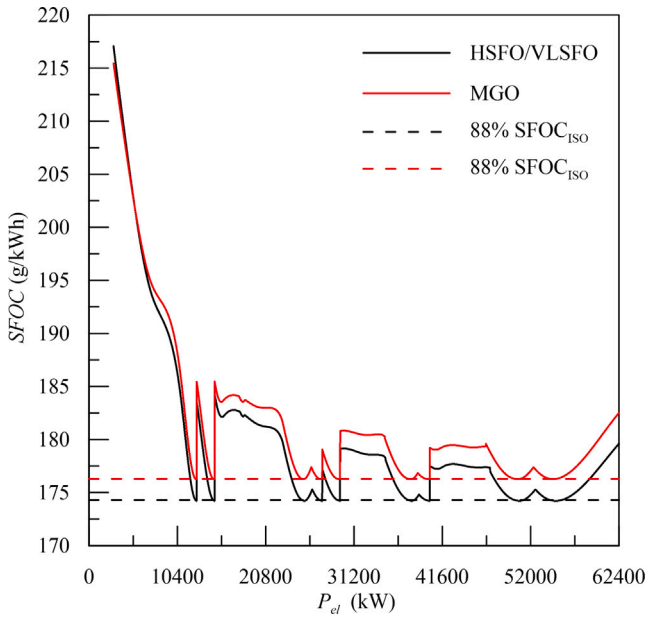

Fig. 14. Onboard power plant SFOC as a function of total required mechanical power in Optimized PMS configuration.

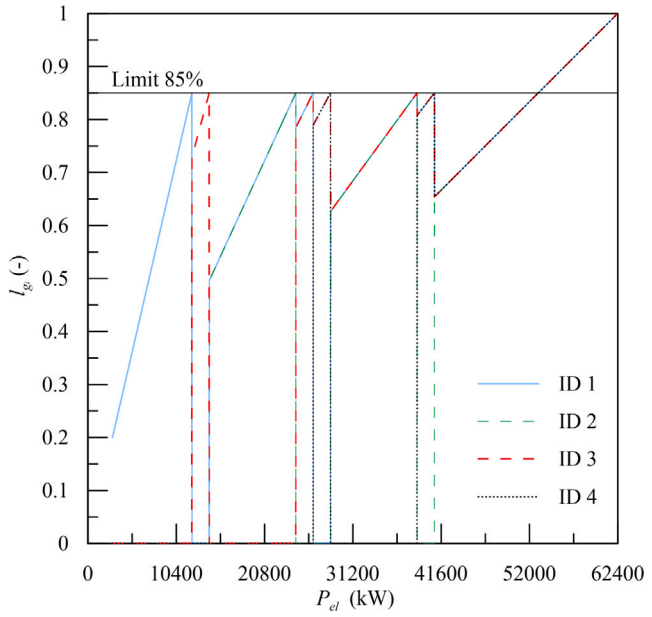

Fig. 15. Load of generators as a function of total required mechanical power in standard PMS configuration.

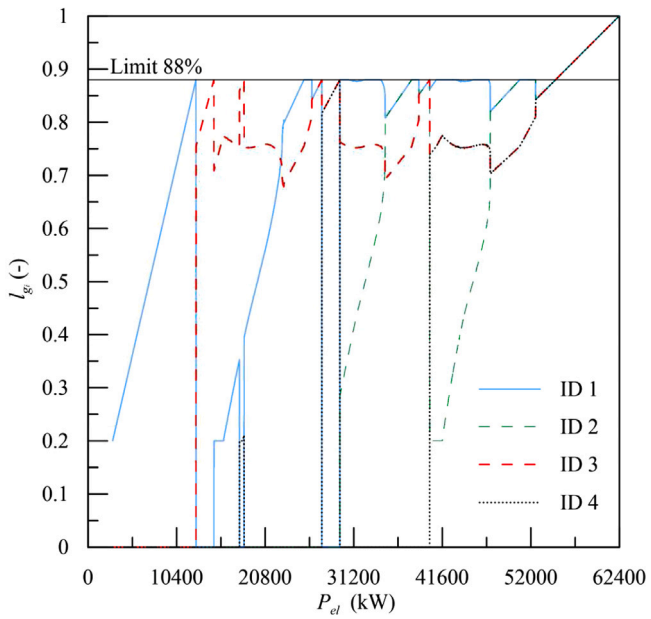

Fig. 16. Load of generators as a function of total required mechanical power in optimized PMS configuration.

6.2. Validation

To validate the simulation physical model, data from the voyage reports of the test ship were compared with individual deterministic simulations on the original itinerary (It. I). Three one-week cruises were considered, simulating one per month from June to August 2022, to represent both pre- and post-dry-dock conditions. The effective wave height, zero-crossing period and direction, sea surface temperature, salinity, air temperature, air density, wind speed and direction assumed in simulations are the actual values for the considered period taken from the EU Copernicus database (Copernicus Marine Service, 2024). Average currents were considered according to the pilot chart (June) without Gaussian noise. Figs. 17, 18, 19 provide the assumed speed profile of the ship along the validation itinerary (It. I). Additionally, to capture the combined effect of environmental factors, the speed profile of the longitudinal component of current relative speed u_{r_c} and angle α' have been included in the same figure. Figs. 20, 21, and 22 provide the comparison between simulated and actual electric energy demand for propulsion (E_{prop}) and other users (E_{others}), obtained from simulation by integrating over time P_{prop} and P_{other}, respectively, as defined in Section 3.1.3. Figs. 23, 24, and 25 depict the comparison between the simulated tank contents and the actual values recorded at port arrival and departure. It is noteworthy that in July, VLSFO was bunkered in Civitavecchia, and in August, MGO was bunkered in Valencia, resulting in a significant increase in fuel quantity between arrival and departure. This has been simulated by disabling the automatic bunkering procedure and manually adding the actual bunkered amount of fuel based on the voyage report upon ship departure.

Concerning propulsion energy, there is a very good match between experimental and simulated data, with a maximum error lower than 2.9%. Additionally, the energy consumption of other loads is also in good agreement, although the value is somewhat underestimated in June and August by simulation, up to 3.5%. These results ensure that the ship's propulsion and chiller power demand are modelled with sufficient accuracy for the purpose of this study.

The simulated fuel consumption aligns well with actual data, with the maximum error observed on VLSFO in August, where the tank filling is overestimated by about 63 t at the end of the itinerary. Although no significant issues related to engine failure or maintenance were reported, the discrepancy in the types of fuel consumed may be attributed to the choices made by the engineering officers in selecting active generators, which might differ from the PMS map. Indeed, when comparing the overall fuel tanks' filling, errors are always below 3%. These results confirm the good accuracy in modelling the onboard standard PMS map, which was employed during validation.

Finally, the filling factors for FW have been qualitatively reproduced. However, since data on onboard passengers were lacking, an accurate estimation of the consumption was challenging, leading to errors of up to −5.8%. Nevertheless, errors regarding overall produced fresh water are −1.9%, 5.2%, −5.3% in June, July, and August, respectively, confirming the sufficient accuracy in modelling evaporators.

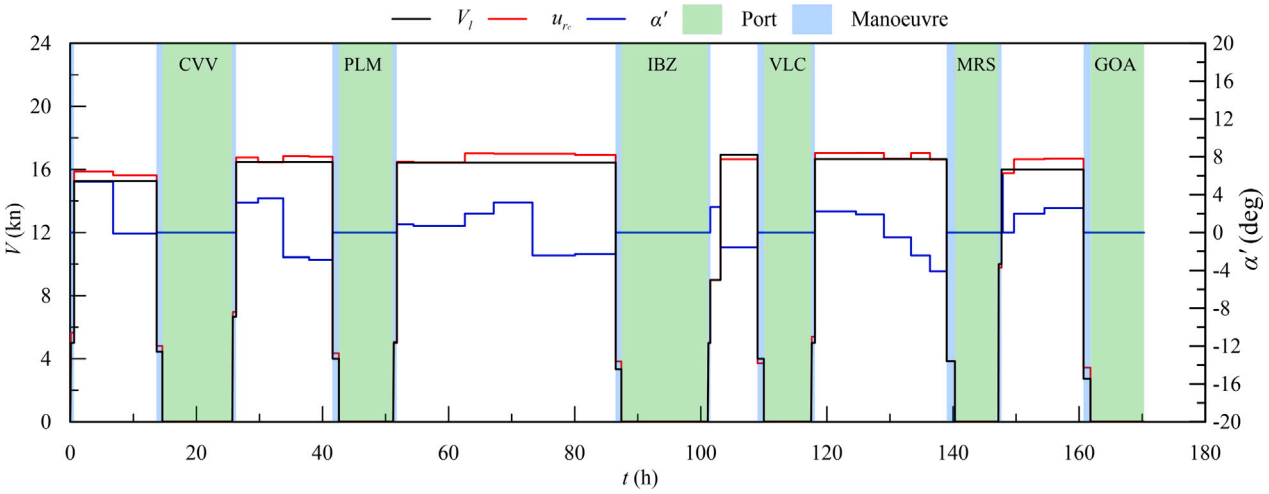

Fig. 17. Assumed speed profile V_l compared with u_{r_c} and angle α' of the ship in validation itinerary (It. I) in June.

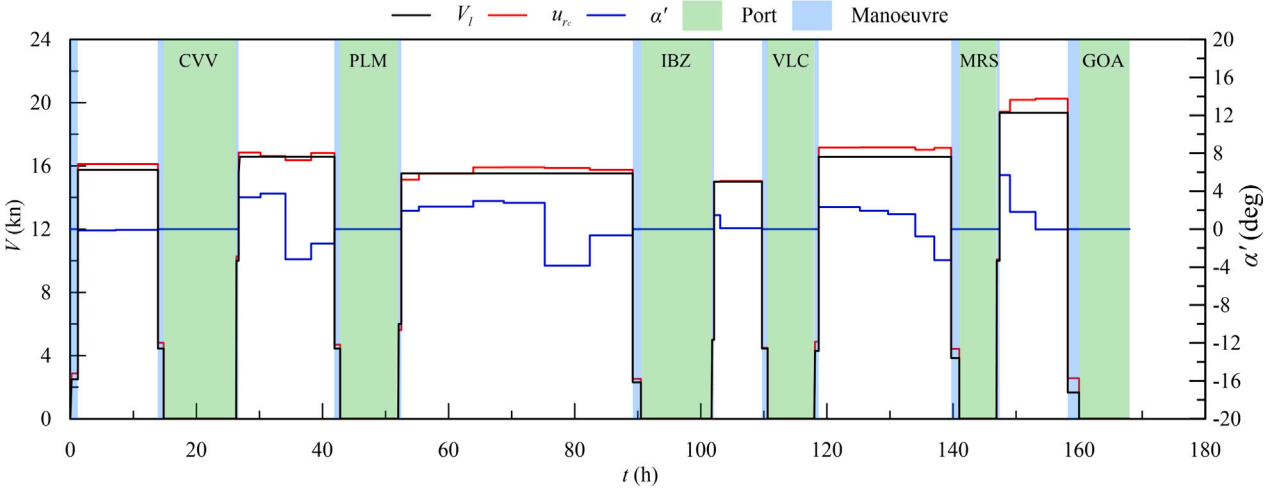

Fig. 18. Assumed speed profile V_l compared with u_{r_c} and angle α' of the ship in validation itinerary (It. I) in July.

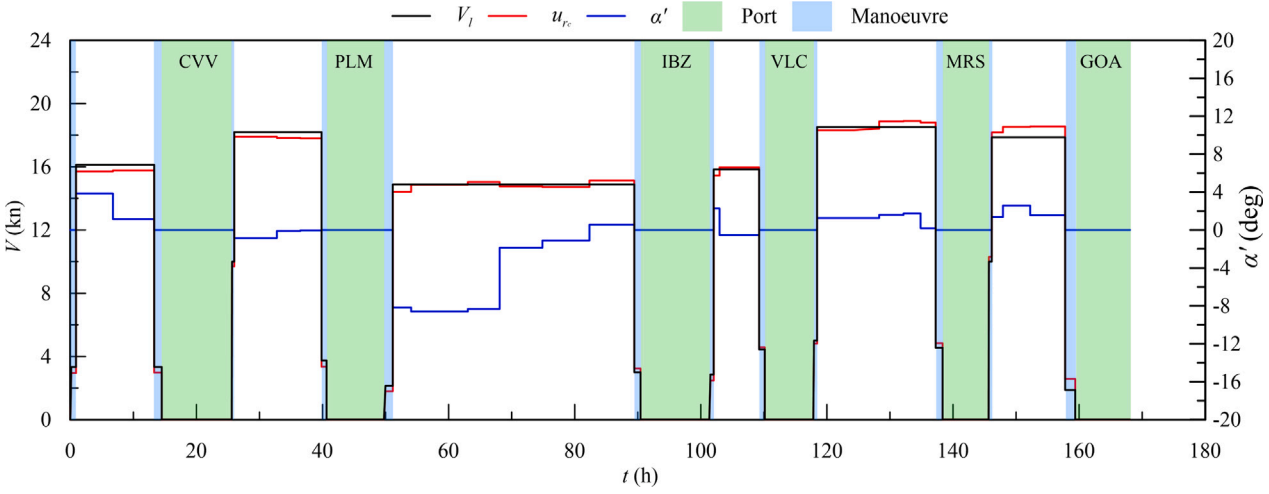

Fig. 19. Assumed speed profile V_l compared with u_{r_c} and angle α' of the ship in validation itinerary (It. I) in August.

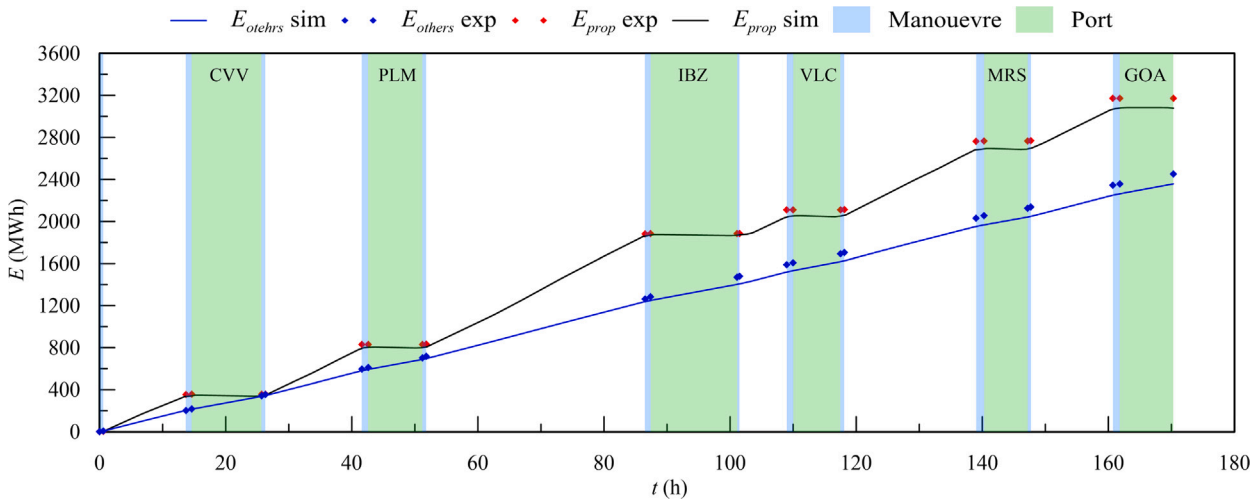

Fig. 20. Simulated (sim) and actual (exp) energy demand in June.

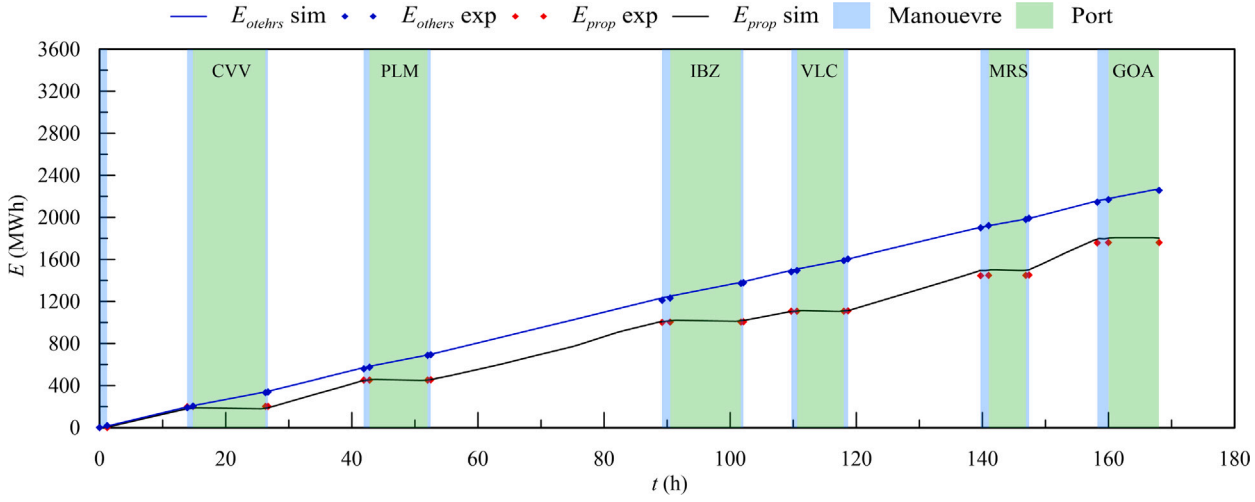

Fig. 21. Simulated (sim) and actual (exp) energy demand in July.

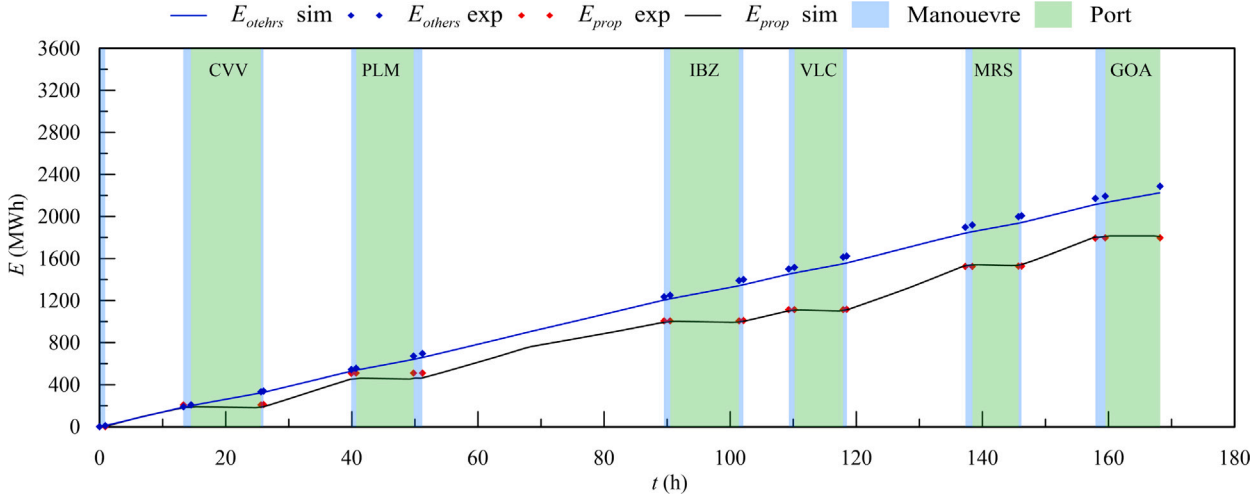

Fig. 22. Simulated (sim) and actual (exp) energy demand in August.

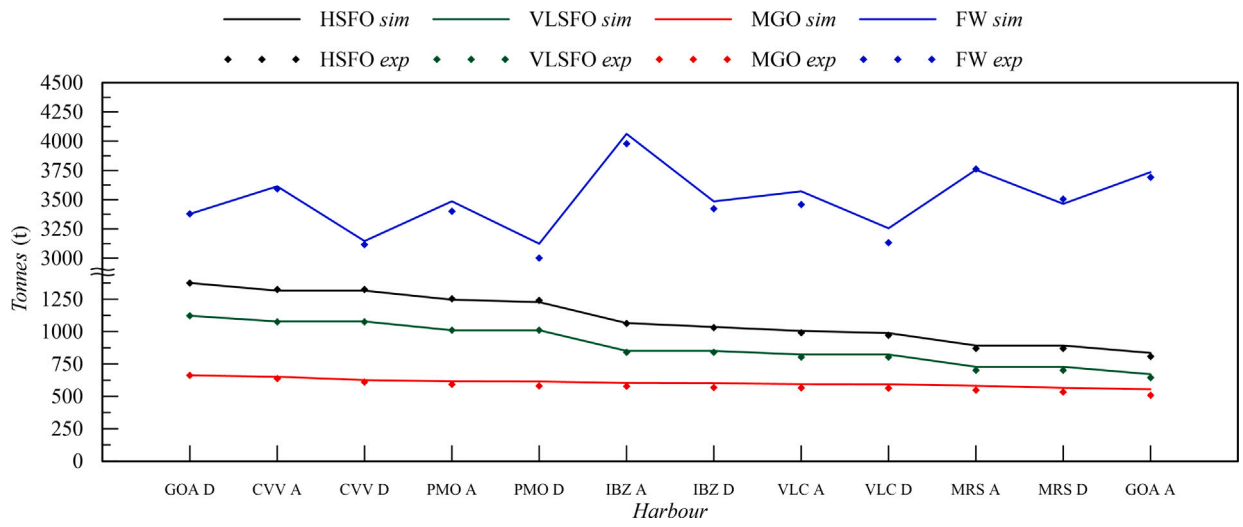

Fig. 23. Simulated (sim) and actual (exp) fuel and FW tanks content in June.

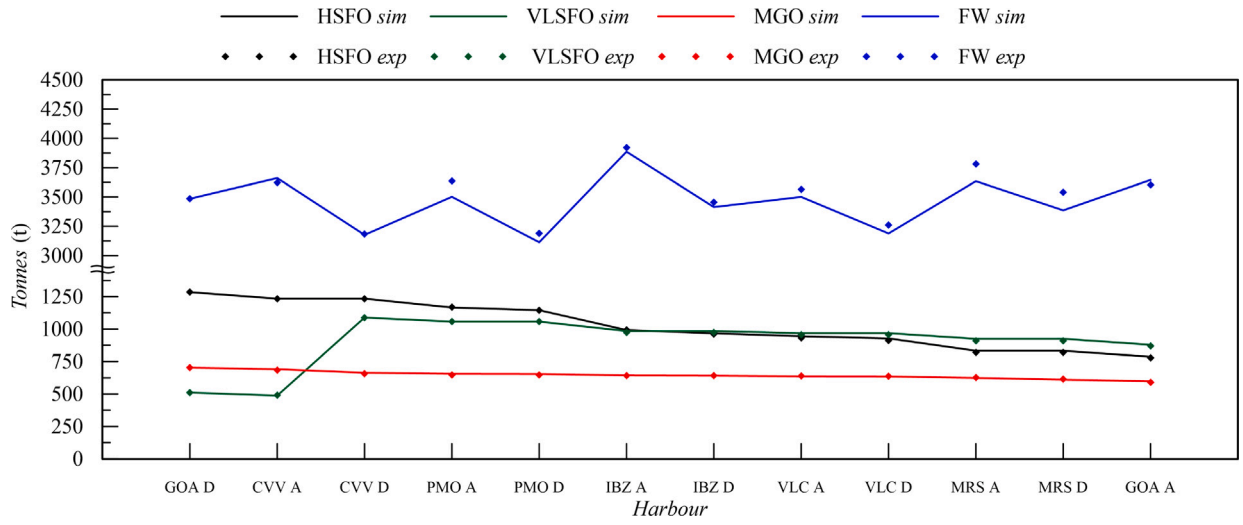

Fig. 24. Simulated (sim) and actual (exp) fuel and FW tanks content in July.

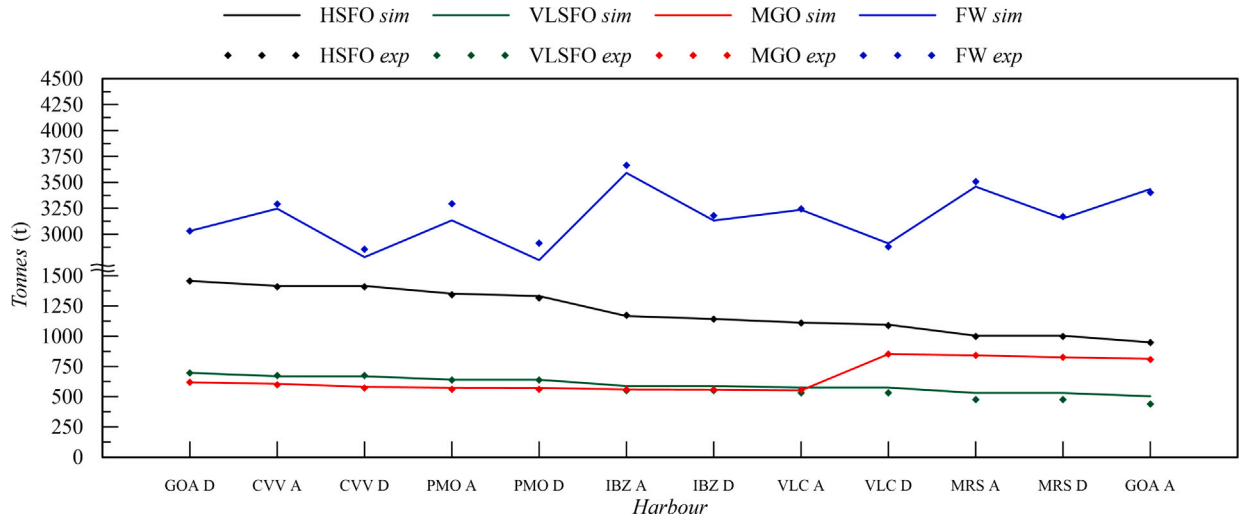

Fig. 25. Simulated (sim) and actual (exp) fuel and FW tanks content in August.

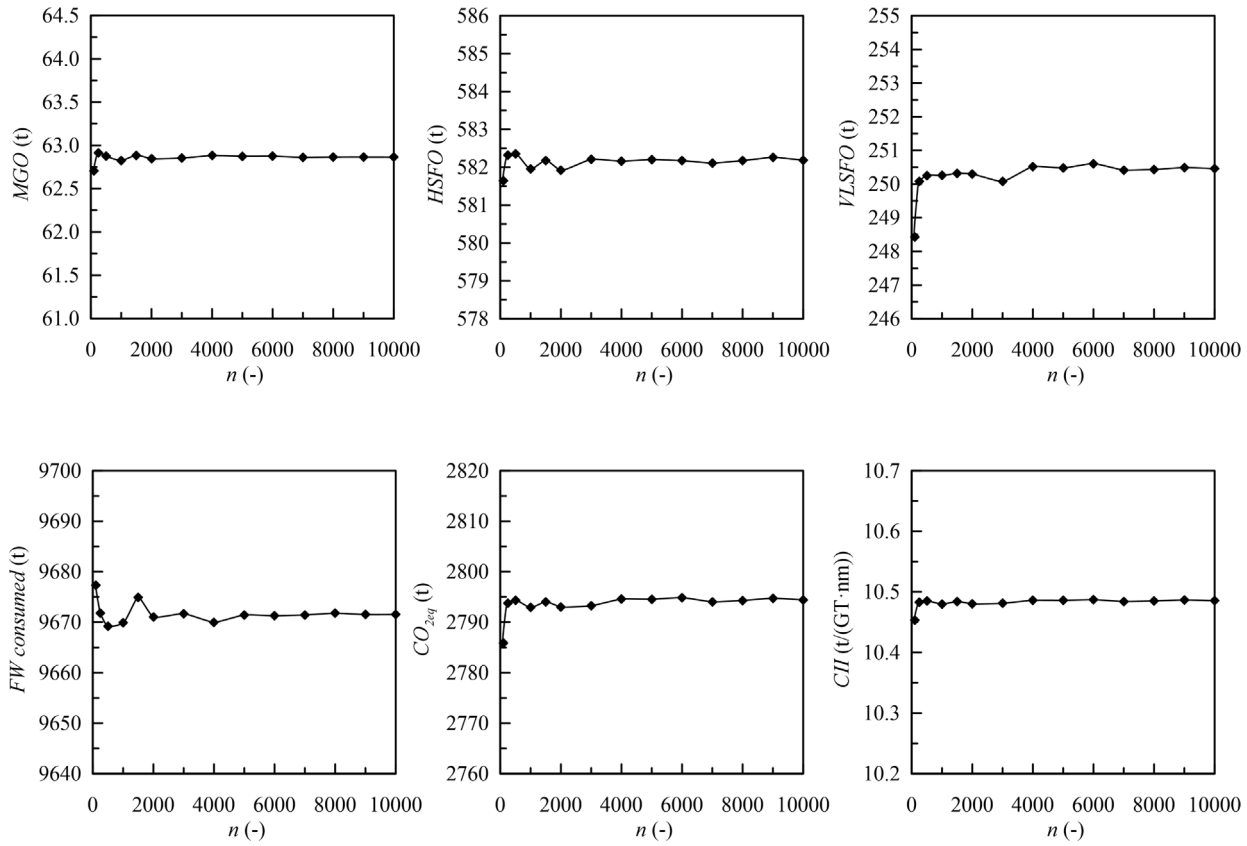

Fig. 26. Median of the main simulated quantities as a function of the number of deterministic scenarios.

In conclusion, the authors consider the validation of the physical simulation model satisfactory; the model is capable of reproducing, with good accuracy, the behaviour of the ship's propulsion system and main machinery on the test itinerary.

6.3. Sensitivity to the number of scenarios

To ensure the accuracy of the probabilistic results, a sensitivity analysis has been conducted. This involved varying the number of generated deterministic scenarios used to assess the median of the most relevant studied quantities in the original itinerary (It. I). The results are presented in Fig. 26. It is noteworthy that the results exhibit good convergence above 3000 scenarios in comparison with the results obtained employing 10000 scenarios. At this point, the maximum deviation observed is approximately 0.15% on VLSFO overall consumption. Consequently, in the following, all the test itineraries have been assessed using 3000 deterministic simulations.

6.4. Simulations results

In the following, the results of simulations are provided encompassing 3000 deterministic scenarios for each of the 5 test itineraries in July 2024. The results include probability distributions and key statistical measures such as mean (μ), median (Q_2), and 3rd quartile (Q_3) for all pertinent quantities. Data are provided highlighting the absolute and percentual difference regarding the original itinerary (It. I), denoted respectively with Δ and e.

Fig. 27 and Table 6 show the outcomes related to MGO consumption. All distributions are nearly symmetric with comparable standard deviations. MGO is utilized by the aft engines in port (at berth and during manoeuvring) and within the last/first 3 nm before-arrival/after-departure. Therefore, freshwater production has minimal impact as it is always deactivated in port (where most MGO consumption occurs).

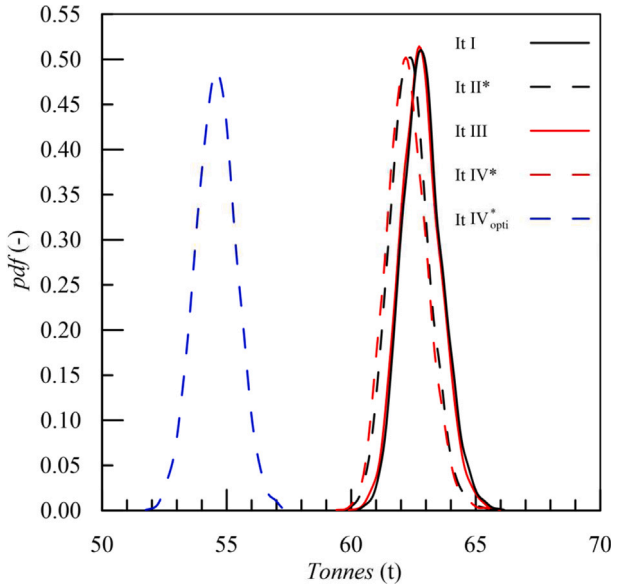

Fig. 27. Probability density functions of MGO consumption in the considered itineraries.

Reversing the itinerary also has a minor effect (approximately 0.5 t per cycle), so the most significant reduction in MGO consumption can be achieved through PMS optimization (approximately 8.5 t per cycle).

Fig. 28 and Table 7 show the outcomes related to HSFO consumption. The distributions are multimodal with relatively short tails. Since HSFO is consistently used by the fore engines equipped with scrubbers, both freshwater production and a reversed schedule contribute

Table 6
MGO consumption for the considered itineraries.

It	μ (t)	Q_2 (t)	Q_3 (t)	Δ_μ (t)	Δ_{Q_2} (t)	Δ_{Q_3} (t)	e_μ (%)	e_{Q_2} (%)	e_{Q_3} (%)
I	62.9	62.8	63.4	–	–	–	–	–	–
II*	62.3	62.3	62.9	−0.5	−0.5	−0.5	−0.8	−0.8	−0.8
III	62.8	62.8	63.3	−0.1	−0.1	−0.1	−0.1	−0.1	−0.1
IV*	62.2	62.2	62.8	−0.6	−0.6	−0.6	−1.0	−1.0	−1.0
IV^*_{Opti}	54.6	54.6	55.1	−8.3	−8.3	−8.3	−13.2	−13.1	−13.0

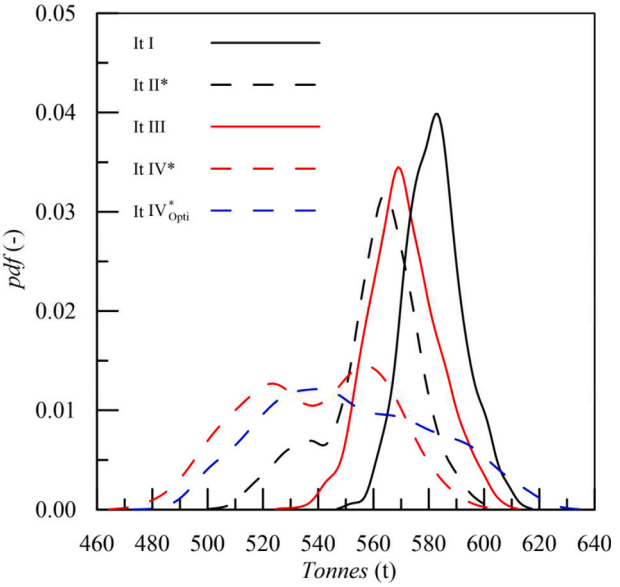

Fig. 28. Probability density functions of HSFO consumption in the considered itineraries.

Table 7
HSFO consumption for the considered itineraries.

It	μ (t)	Q_2 (t)	Q_3 (t)	Δ_μ (t)	Δ_{Q_2} (t)	Δ_{Q_3} (t)	e_μ (%)	e_{Q_2} (%)	e_{Q_3} (%)
I	582.1	581.7	588.6	–	–	–	–	–	–
II*	560.0	562.6	571.1	−22.1	−19.2	−17.6	−3.8	−3.3	−3.0
III	570.9	570.3	579.2	−11.1	−11.5	−9.4	−1.9	−2.0	−1.6
IV*	538.4	539.6	559.1	−43.7	−42.2	−29.6	−7.5	−7.3	−5.0
IV^*_{Opti}	551.7	549.1	574.8	−30.4	−32.6	−13.9	−5.2	−5.6	−2.4

to reducing average fuel consumption. The itinerary reversal has the greatest impact (approximately 25 t per cycle). The PMS optimization process generally results in higher power demand from the fore engines (see loads of engines 1 and 3 in Figs. 15 and 16), thus, the average HSFO consumption in Itinerary IV^*_{Opti} is about 13 t higher than in Itinerary IV*. However, this increase is largely offset by the reduced consumption of MGO and VLSFO in the optimized configuration, as discussed later on.

Fig. 29 and Table 8 show the outcomes related to VLSFO consumption. These distributions exhibit strong asymmetry with a longer right tail. Similar to HSFO, itinerary reversal has a more pronounced impact on reducing VLSFO consumption compared to turning off freshwater production. In contrast to HSFO but similar to MGO, the PMS optimization process results in reduced power demand from aft engines (which predominantly use VLSFO during navigation), achieving a reduction of approximately 33 t per cycle when comparing Itinerary IV* and Itinerary IV^*_{Opti}.

The aggregated fuel consumption is provided in Fig. 30 and Table 9, and overall emissions are provided in Fig. 31 and Table 10. These distributions are largely unimodal and asymmetric with a longer right tail. All modifications tested on the original itinerary have a positive impact

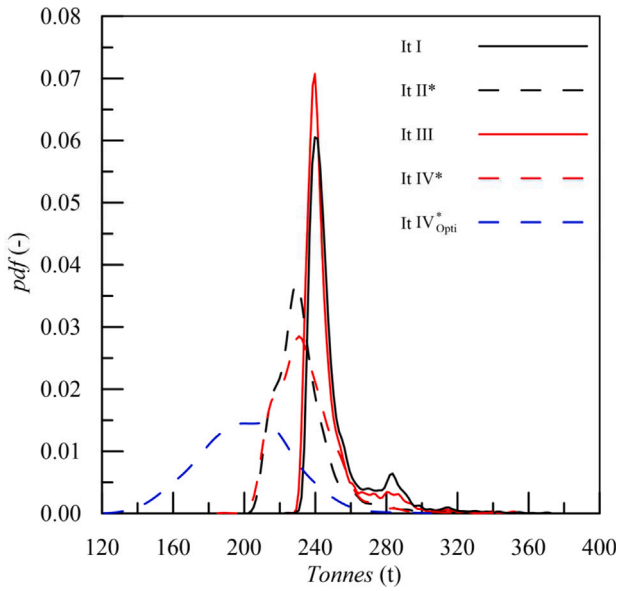

Fig. 29. Probability density functions of VLSFO consumption in the considered itineraries.

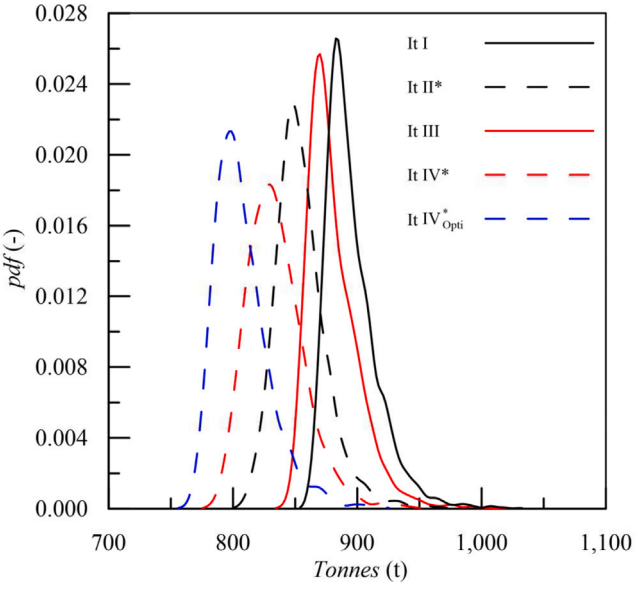

Fig. 30. Probability density functions of total fuel consumption in the considered itineraries.

Table 8
VLSFO fuel consumption for the considered itineraries.

It	μ (t)	Q_2 (t)	Q_3 (t)	Δ_μ (t)	Δ_{Q_2} (t)	Δ_{Q_3} (t)	e_μ (%)	e_{Q_2} (%)	e_{Q_3} (%)
I	250.4	243.9	252.7	–	–	–	–	–	–
II*	232.5	230.2	238.7	−17.9	−13.7	−14.0	−7.1	−5.6	−5.5
III	246.6	241.5	248.2	−3.8	−2.4	−4.5	−1.5	−1.0	−1.8
IV*	233.7	232.0	242.5	−16.6	−11.9	−10.2	−6.6	−4.9	−4.0
IV^*_{Opti}	200.9	201.1	218.6	−49.5	−42.8	−34.1	−19.8	−17.5	−13.5

on reducing fuel consumption and emissions. Specifically, comparing the original itinerary with the optimized one, average Tank-to-Wake emissions can be reduced by approximately 10%. This improvement also positively affects the CII, as depicted in Fig. 32, which illustrates the probability of the ship being classified according to the CII in the studied itineraries. These results are derived by applying the CII

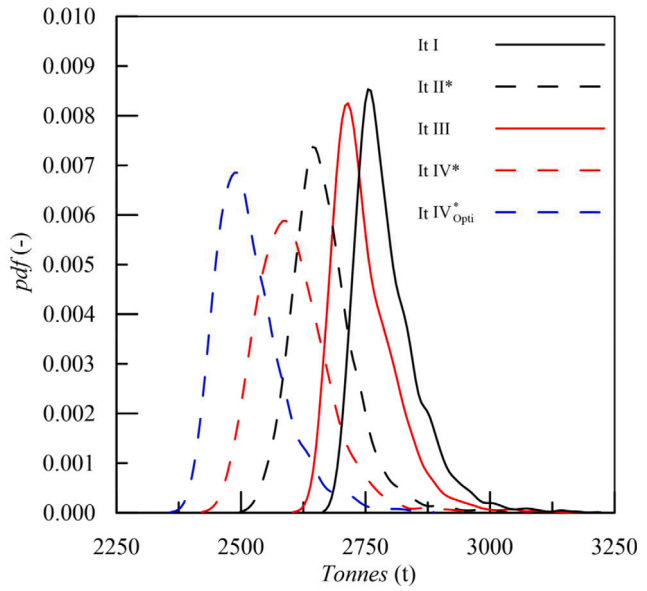

Fig. 31. Probability density functions of equivalent CO_2 emissions in the considered itineraries.

thresholds for the year 2024 to the emissions associated with each deterministic scenario to determine the corresponding CII class. Subsequently, the percentages shown in the pie charts across all studied itineraries are computed based on all scenarios.

7. Discussion

The validation process underscores the significant impact of fouling on cruise ships, as evidenced by variations in fuel consumption. In June (Fig. 23), prior to the dry-dock, the ship consumed approximately 1100 t of fuel. However, after the dry-dock in July (Fig. 24) and August (Fig. 25), with a clean hull and propeller, the fuel consumption noticeably decreased to about 800 t. This substantial variation is primarily attributed to the extended stop during the COVID-19 pandemic. Nonetheless, the fouling effect on cruise ships raises critical considerations, especially regarding economic implications: during a dry-dock, the ship incurs additional costs without generating revenue. Investigating propeller and hull polishing patterns between dry-docks could offer valuable insights into mitigating fouling effects. However, hull polishing alone does not prevent immediate biofouling accumulation, making it less effective than a dry-dock over the long term. This complex scenario necessitates a comprehensive analysis to optimize dry-dock/polishing schedules, although this falls beyond the scope of the present work. Such practices could contribute to more sustainable and efficient ship operations.

Table 9
Total fuel consumption for the considered itineraries.

It	μ (t)	Q_2 (t)	Q_3 (t)	Δ_μ (t)	Δ_{Q_2} (t)	Δ_{Q_3} (t)	e_μ (%)	e_{Q_2} (%)	e_{Q_3} (%)
I	895.3	890.5	905.5	–	–	–	–	–	–
II*	854.8	852.1	865.7	−40.5	−38.4	−39.8	−4.5	−4.3	−4.4
III	880.3	875.8	891.1	−15.0	−14.7	−14.4	−1.7	−1.7	−1.6
IV*	834.3	831.9	847.9	−60.9	−58.6	−57.7	−6.8	−6.6	−6.4
IV^*_{Opti}	807.1	803.2	818.7	−88.2	−87.3	−86.9	−9.9	−9.8	−9.6

Table 10
Overall equivalent CO_2 consumption for the considered itineraries.

It	μ (t)	Q_2 (t)	Q_3 (t)	Δ_μ (t)	Δ_{Q_2} (t)	Δ_{Q_3} (t)	e_μ (%)	e_{Q_2} (%)	e_{Q_3} (%)
I	2794	2779	2826	–	–	–	–	–	–
II*	2668	2659.2	2702	−126.2	−119.6	−124.1	−4.5	−4.3	−4.4
III	2747	2733	2781	−46.7	−45.8	−45.0	−1.7	−1.6	−1.6
IV*	2604	2596	2646	−189.8	−182.7	−179.6	−6.8	−6.6	−6.4
IV^*_{Opti}	2518	2506	2554	−275.4	−272.6	−271.2	−9.9	−9.8	−9.6

Shifting focus to itinerary planning, the feasibility of the proposed itinerary becomes a crucial consideration for operational planning at a strategic level. An itinerary may face technical infeasibility if there is a risk of the ship running out of fuel or FW during a leg or experiencing delays due to adverse weather conditions. The proposed methodology enables the evaluation of delay risk for each subleg and, similarly, assesses the risk of fuel stocks falling below a safety threshold upon arrival. This helps identify critical legs and sublegs, facilitating a proactive identification of potential disruptions during itinerary planning, and adjustments to the original itinerary to mitigate their consequences. This kind of analysis serves as a foundational aspect for future applications of the methodology in diverse cruise scenarios. However, in the context of the test itineraries, no critical issues arose, confirming the complete feasibility of both the original itinerary and its variants.

Having established the feasibility of the itineraries, the analysis now shifts to examining the impact of the changes made to the original itinerary on emissions. Notably, the reversal of the itinerary in Itineraries II* and IV* emerges as a strategic decision, resulting in substantial fuel and emissions savings. As emerges from data in Tables 9 and 10, in July alone, a significant average reduction of approximately 41 t of fuel and 126 tCO_2e can be achieved weekly. This notable outcome is primarily attributed to leveraging ocean currents, which predominantly favour the reversed itinerary.

The probability distributions of emissions (Fig. 31) exhibit non-normality, demonstrating comparable variance and small positive skewness. Consequently, the right tail of the distribution is longer than the left one. This observation is particularly relevant for itinerary planning, where the analysis of the right tail can help determine the risk of exceeding specific values in emissions and/or fuel consumption. This information is crucial for budgeting purposes, particularly in managing

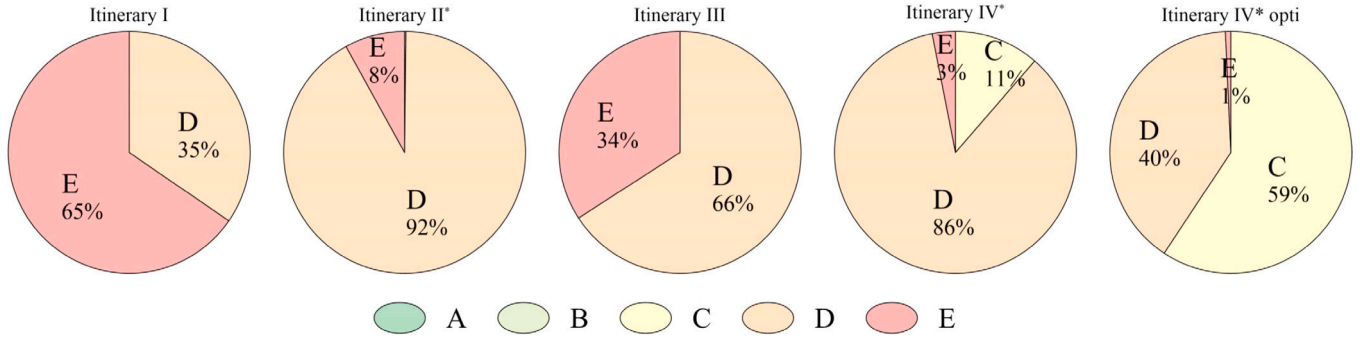

Fig. 32. Probability of obtaining a *CII* rating in the studied itineraries.

the risk associated with the advance purchase of CO_2 allowances on ETS, needed when the itinerary includes EU ports. This approach ensures the avoidance of acquiring an unreasonably large amount of allowances (i.e., immobilized capital) or too few (resulting in costly sanctions).

In the reversed itinerary (Itinerary IV*), where FW production is switched off, an additional 20 t of fuel and 70 tCO_2e can be saved due to the deactivation of reverse osmosis machines (as shown in Tables 9 and 10). However, it should be noted that this decision introduces additional costs as FW must be purchased at ports. On the other hand, if the itinerary involves EU ports, the economic savings are not limited to fuel costs. This leads to emissions reduction, limiting the amount of CO_2 allowances to be purchased on ETS. Therefore, to make an informed decision about whether FW should be produced onboard or purchased at ports, an economic trade-off is again necessary. Nonetheless, the methodology demonstrates its capability to differentiate and thoroughly analyse various alternatives, addressing many uncertainties arising from environmental conditions. This underscores its potential usefulness in enhancing cruise itineraries for environmental sustainability and economic benefits as well.

Moreover, this study underscores the potential of PMS optimization as a powerful tool for emissions control. This is exemplified by a significant average reduction of 27 t of fuel and 85.6 tCO_2e in Itinerary IV^*_{Opt} compared to Itinerary IV*, utilizing the standard PMS configuration (see Tables 9 and 10). This 3% reduction is solely attributed to the appropriate PMS configuration and can be achieved with relatively inexpensive and limited upgrades to software and hardware. The methodology's capability to pre-test and analyse specific machinery configurations, such as running generators at optimal loads, presents a promising opportunity for cruise operators to embrace more sustainable practices.

Variations in emissions along the studied itineraries also influenced the CII classification. As illustrated in Fig. 32, the original itinerary exhibits poor CII performance: in two-thirds of the simulated scenarios, the ship is classified as E, while the remainder falls into class D. According to IMO regulations, a vessel assigned a D rating for three consecutive years or an E rating for a single year must submit a corrective action plan, outlining steps to achieve the required index of C or higher. In this context, the proposed methodology can be instrumental in supporting activities aimed at enhancing the environmental performance of the ship. For instance, the reversal of the itinerary and PMS optimization jointly result in a 59% probability of classifying the ship as class C, without modifying the ship's speed or the duration of port stays. It is noteworthy that for cruise vessels, which often have significant fuel consumption at berth, improving CII performance might involve reducing port stays (potentially diminishing the appeal of cruises) or increasing ship speed to cover longer distances (resulting in higher CO_2 emissions). None of these potentially questionable practices were considered in this study to improve the CII class.

A more in-depth analysis explores the probability density functions ($pdfs$) for individual fuel types . In contrast to the unimodal pdf for overall fuel consumption (Figs. 30), $pdfs$ for two individual fuels reveal multimodality (Figs. 28 and 29). This results from the different sets of active generators required by variable power demands from the power plant, coupled with the fact that forward generators can use HSFO, while aft ones shall use VLSFO/MGO. The different configurations of active generators also affect their motion hours. Indeed, the motion hours of generators vary significantly depending on the PMS configuration and engine type. In general, optimized PMS leads to a reduction in the motion hours of aft generators (those without scrubbers), as noted by the reduced consumption of MGO and VLSFO in Itinerary IV^*_{Opti} (Figs. 27 and 29). Besides, they lead to slightly increased motion hours of generators employing HSFO (Fig. 28). Possible extraction of motion hours $pdfs$ of the main machinery from simulations, since the itinerary planning, could be useful for anticipating periodic maintenance planning and refining the simulation model to account for it (e.g., considering the probability of having an engine down for maintenance).

Decomposing the mean electric power demand, as shown in Fig. 33, offers valuable insights into the substantial contribution of propulsion during navigation. This share has increased in recent decades due to the introduction of new, more efficient technologies such as chillers with inverters and LED lighting. Nevertheless, auxiliaries and chillers are confirmed as significant contributors to power demand, opening avenues for targeted efficiency improvements. Reversing the itinerary, mainly impacts propulsion and auxiliaries' power demand, with a reduction of about 2.26 MW and 0.175 MW, respectively. Auxiliaries' power demand is evidently affected also by FW production.

Further decomposition of average emissions by phase (Table 11) reveals that the majority stem from port stay and navigation. This insight justifies the decision not to simulate the manoeuvring phase with high accuracy during itinerary planning, given its modest impact. However, this simplification might introduce potential systematic errors, urging cruise operators to balance accuracy with computational efficiency, which will increase if more complex simulation methods are adopted while being driven by MC sampling. Currently, the proposed methodology requires a computational time of about 180 min for 3000 simulations on a cluster equipped with an Intel(R) Xeon(R) Gold 5118 @2.30 GHz CPU, performing 48 parallel simulation processes. The average time required for a single simulation performed by one of the CPU's cores is thus approximately 173 s, which is much faster than any manoeuvring or numerical simulation codes.

8. Conclusions

The paper introduced a probabilistic methodology to address the environmental challenges of modern itinerary planning faced by cruise companies. It is based on a physical simulation model that aligns well with full-scale experimental data, driven by MC sampling. The main contributions to the field are twofold. First, it overcomes the technical limitations of the methods currently employed in cruise itinerary planning to provide more realistic fuel consumption and emissions forecasts. Second, it defines a simple, fast, and reliable simulation model specialized for cruise ships, which was previously lacking in the existing literature. The relevance and potential of the proposed technique in reducing emissions have been proven on a real West-Med itinerary, which has been simulated in multiple variants with the following main outcomes:

- In July, environmental conditions (particularly currents) lead to significant differences in fuel consumption between the original and reversed itineraries of about 5% (130 tCO_2e).
- Onboard FW production leads to higher CO_2 emissions of about 2% (50 tCO_2e).
- PMS optimization results in reduced average emissions of about 3.1% (86 tCO_2e).
- Combining itinerary reversing, no FW production, and PMS optimization, about a 10% reduction in emissions can be achieved (275 tCO_2e).
- In the latter case, a C rating can likely be reached for the Carbon Intensity Indicator (CII), instead of the E rating, which was the most probable for the original itinerary.

Hence, the effectiveness of the proposed methodology in capturing differences induced by these relevant aspects has been deemed satisfactory to show the potential of probabilistic methods during itinerary planning.

Using multiple simulation scenarios randomly generated according to the probability distribution of the main stochastic variables (environmental, related to persons onboard, etc.), the probability density function of key dependent variables (emissions, fuel consumption, FW production/consumption, etc.) can be defined. From these distributions, average values can be extracted leading to a better forecast of the

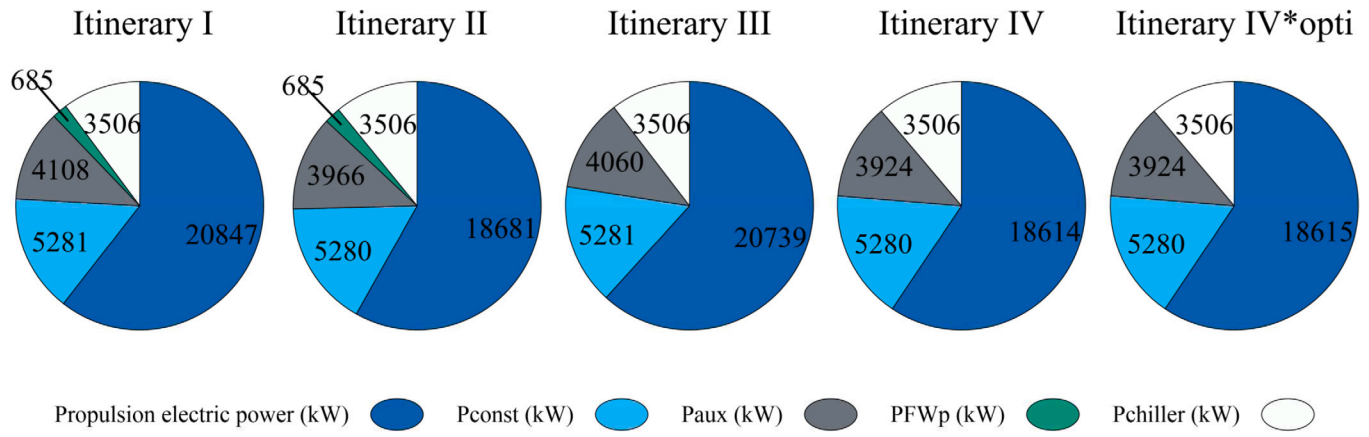

Fig. 33. Average values of electric power demand by category during navigation.

Table 11
Average values of fuel consumption by phase.

It	Fuel	At sea			Canal Transit			Manoeuvre			Port stay		Boiler		Total	
		fc (t)	Dist. (nm)	t (h)	fc (t)	Dist. (nm)	t (h)	fc (t)	Dist. (nm)	t (h)	fc (t)	t (h)	fc (t)	t (h)	fc (t)	fc (t)
	HSFO	464	1687	104	11	28	8	5	5	1	102	47	0	0	582	
I	VLSFO	250	1657	102	0	0	0	0	0	0	0	0	0	0	250	895
	MGO	7	36	2	14	37	9	6	6	2	13	6	23	168	63	
	HSFO	442	1687	104	11	28	8	5	5	1	85	47	0	0	543	
II*	VLSFO	232	1657	102	0	0	0	0	0	0	0	0	0	0	232	838
	MGO	7	36	2	14	37	9	6	6	2	13	6	23	168	62	
	HSFO	453	1687	104	11	28	8	5	5	1	102	47	0	0	571	
III	VLSFO	247	1657	102	0	0	0	0	0	0	0	0	0	0	247	880
	MGO	7	36	2	14	37	9	6	6	2	13	6	23	168	63	
	HSFO	420	1687	104	11	28	8	5	5	1	102	47	0	0	538	
VI*	VLSFO	234	1657	102	0	0	0	0	0	0	0	0	0	0	234	834
	MGO	7	36	2	14	37	9	6	6	2	13	6	23	168	62	
	HSFO	428	1687	104	17	28	8	6	5	1	85	47	0	0	534	
IV^*_{Opti}	VLSFO	201	1657	102	0	0	0	0	0	0	0	0	0	0	201	789
	MGO	6	36	2	8	37	9	5	6	2	13	6	22	168	53	

performance of a specific itinerary under evaluation. Moreover, values related to a predefined risk of exceedance can be also assessed. For instance, in the results, also the values of the third quartile are reported for which the risk of exceedance is 25%. This can allow better risk management when strategic decisions shall be made during itinerary planning.

The simulation process has proven to be relatively fast. In an applied context, not limited to research purposes, the computational time is considered acceptable for comparing alternatives during itinerary planning. However, it is already too high to introduce time-domain simulations or conduct itinerary optimization within a reasonable timeframe. This presents an opportunity for future research to explore additional simplifications or further improvements, moving towards more ambitious goals, such as optimizing waypoints within an itinerary or better predicting the electric power demand from chillers or other auxiliaries.

From a pragmatic standpoint within the cruise company context, it will be advisable to embrace a more advanced approach to itinerary planning that considers both environmental and economic factors. In this regard, further studies are recommended to analyse the economic impact of strategic choices made in itinerary planning. This includes considerations related to main machinery operation, maintenance, FW production/purchase policies, with a specific focus on itineraries calling at EU ports, thus necessitating the acquisition of CO_2 allowances on ETS. Besides, in accordance with IMO strategy, Well-to-Tank emissions should also be considered to integrate with the Tank-to-Wake emissions that can be assessed by the current simulation model.

Future work is also needed to improve the simulation model and data sources. First, an experimental campaign collecting time records of the main ship parameters could be conducted to enhance the model's validation, including a thorough analysis of each environmental aspect and related uncertainties. Regarding the datasets and their statistical elaboration, the employed sources and methods have been deemed sufficient to demonstrate the potential of the proposed technique for itinerary planning, but it should be noted that there is still significant room for improvement to increase the reliability of model predictions. In particular, future work is required to integrate data from more recent and accurate databases (based on hindcast ocean models), to distinguish between local waves and swell, to capture correlations between different environmental parameters, e.g., define more realistic wind–wave relationships, define connections between sea and air temperatures, and introduce air humidity. Additionally, the model might be improved to better capture the physics of the main ship systems: currently, only the most important one (i.e., the propulsion system) has been modelled in detail, whereas for the other systems, design data owned by cruise companies have been used to facilitate the model's application in an operational environment. Nonetheless, prediction accuracy might benefit from more detailed modelling of air conditioning systems and the most important auxiliaries.

Founding

This study was carried out within the consortium iNEST (Interconnected North-Est Innovation Ecosystem) CUP J43C22000320006 funded by the European Union Next-GenerationEU (Piano Nazionale di Ripresa e Resilienza (PNRR)—Missione 4 Componente 2, Investimento 1.5—D.D. 1058 23/06/2022, ECS_00000043). This manuscript reflects only the Authors' views and opinions.

CRediT authorship contribution statement

Luca Braidotti: Writing – original draft, Validation, Supervision, Software, Project administration, Methodology, Funding acquisition, Conceptualization. **Samuele Utzeri:** Writing – original draft, Visualization, Software, Investigation, Formal analysis, Data curation. **Serena Bertagna:** Writing – review & editing, Validation, Resources, Project administration, Methodology, Funding acquisition. **Vittorio Bucci:** Writing – review & editing, Visualization, Supervision, Project administration, Funding acquisition.

Declaration of competing interest

The authors declare the following financial interests/personal relationships which may be considered as potential competing interests: Luca Braidotti reports financial support was provided by European Union. If there are other authors, they declare that they have no known competing financial interests or personal relationships that could have appeared to influence the work reported in this paper.

Acknowledgements

The work was realized with the support of Marinelab d.o.o. for sharing their technical expertise, which greatly helped in defining reliable assumptions for the simulation model.

Appendix A. Relative speed

To assess the environmental forces related to current and wind acting on the ship, it is necessary to evaluate the relative speed and its angle, which account for the course and speed of the ship. The ship is moving at a speed V_l along the true course identified by the angle α from the North direction.

The heading of the ship (direction of the bow), defining the ship-fixed reference system, is identified by the angle ψ from the North direction. The angle α' between the heading and the course is then defined as:

$$\alpha' = \alpha - \psi \tag{46}$$

Considering a generic environmental parameter e (current or wind) with a speed over the ground V_e and a direction θ from the North, the angle between the ship's heading and V_e is:

$$\theta' = \theta - \psi \tag{47}$$

Hence, the longitudinal and transversal components of the relative speed in the ship-fixed reference system are given by:

$$\begin{aligned} u_{r_e} &= V_l \cos\alpha' - V_e \cos\theta' \\ v_{r_e} &= V_l \sin\alpha' - V_e \sin\theta' \end{aligned} \tag{48}$$

and the relative speed V_{r_e} and is angle from the heading θ'_r is, then, given by:

$$\begin{aligned} V_{r_e} &= \sqrt{u_{r_e}^2 + v_{r_e}^2} \\ \theta'_r &= -\operatorname{atan2}(v_{r_e}, u_{r_e}) \end{aligned} \tag{49}$$

The negative sign of arctangent is determined according to the definitions used in Blendermann (2014), Fossen (2011)

Appendix B. Itinerary detailed schedule

In Table 12, the detailed schedule of the original itinerary is presented. Specifically, it illustrates how the itinerary has been divided into sublegs for both validation and simulation purposes.

Table 12
Detailed Schedule and discretization of original itinerary.

nSubLeg	Type	Leg	ψ (deg)	length (nm)	Δt (h)	V_l (kn)
1	Port Stay	GOA	0	0	0	0
2	Manoeuvring	GOA	161	0.5	0.2	2.5
3	Transit	GOA→CVV	161	2.5	1	2.5
4	Navigation	GOA→CVV	161	3	0.2	15.7
5	Navigation	GOA→CVV	161	91.4	5.8	15.7
6	Navigation	GOA→CVV	117	102.6	6.5	15.7
7	Navigation	GOA→CVV	117	3	0.2	15.7
8	Transit	GOA→CVV	117	3.5	0.8	4.4
9	Manoeuvring	CVV	117	0.5	0.1	4.4
10	Port Stay	CVV	0	0	11.5	0
11	Manoeuvring	CVV	182	0.5	0.1	10
12	Transit	CVV→PLM	182	3.5	0.4	10
13	Navigation	CVV→PLM	181	3	0.2	16.6
14	Navigation	CVV→PLM	181	54.3	3.3	16.6
15	Navigation	CVV→PLM	181	65.7	4	16.6
16	Navigation	CVV→PLM	158	67.7	4.1	16.6
17	Navigation	CVV→PLM	141	58.3	3.5	16.6
18	Navigation	CVV→PLM	141	3	0.2	16.6
19	Transit	CVV→PLM	141	3.5	0.8	4.4
20	Manoeuvring	PLM	141	0.5	0.1	4.4
21	Port Stay	PLM	0	0	9.2	0
22	Manoeuvring	PLM	281	0.5	0.1	6
23	Transit	PLM→IBZ	281	2.5	0.4	6
24	Navigation	PLM→IBZ	281	3	0.2	15.5
25	Navigation	PLM→IBZ	281	40.4	2.6	15.5
26	Navigation	PLM→IBZ	273	133.8	8.6	15.5
27	Navigation	PLM→IBZ	269	75.1	4.8	15.5
28	Navigation	PLM→IBZ	272	100.9	6.5	15.5
29	Navigation	PLM→IBZ	279	111	7.1	15.5
30	Navigation	PLM→IBZ	281	102.8	6.6	15.5
31	Navigation	PLM→IBZ	281	3	0.2	15.5
32	Transit	PLM→IBZ	281	2.5	1.1	2.3
33	Manoeuvring	IBZ	281	0.5	0.2	2.3
34	Port Stay	IBZ	0	0	11.2	0
35	Manoeuvring	IBZ	47	0.5	0.1	5
36	Transit	IBZ→VLC	47	1.5	0.3	5
37	Navigation	IBZ→VLC	47	3	0.2	15
38	Navigation	IBZ→VLC	47	11.7	0.8	15
39	Navigation	IBZ→VLC	280	96.3	6.4	15
40	Navigation	IBZ→VLC	280	3	0.2	15
41	Transit	IBZ→VLC	280	3.5	0.8	4.4
42	Manoeuvring	VLC	280	0.5	0.1	4.4
43	Port Stay	VLC	0	0	7.4	0
44	Manoeuvring	VLC	54	0.5	0.1	4.3
45	Transit	VLC→MRS	54	2.5	0.6	4.3
46	Navigation	VLC→MRS	54	3	0.2	16.6
47	Navigation	VLC→MRS	54	105.3	6.4	16.6
48	Navigation	VLC→MRS	50	73.9	4.5	16.6
49	Navigation	VLC→MRS	41	71.6	4.3	16.6
50	Navigation	VLC→MRS	41	50	3	16.6
51	Navigation	VLC→MRS	45	41.2	2.5	16.6
52	Navigation	VLC→MRS	45	3	0.2	16.6
53	Transit	VLC→MRS	45	4.5	1.2	3.8
54	Manoeuvring	MRS	45	0.5	0.1	3.8
55	Port Stay	MRS	0	0	5.9	0
56	Manoeuvring	MRS	154	0.5	0.1	10
57	Transit	MRS→GOA	154	4.5	0.5	10
58	Navigation	MRS→GOA	154	3	0.2	19.4
59	Navigation	MRS→GOA	154	28.7	1.5	19.4
60	Navigation	MRS→GOA	68	78.2	4	19.4
61	Navigation	MRS→GOA	44	96.1	5	19.4
62	Navigation	MRS→GOA	44	3	0.2	19.4
63	Transit	MRS→GOA	44	2.5	1.5	1.7
64	Manoeuvring	GOA	44	0.5	0.3	1.7
65	Port Stay	GOA	0	0	8	0

References

Ambrosino, D., Asta, V., 2021. An optimization model to help cruise companies to evaluate their offer in a basin. pp. 375–383. http://dx.doi.org/10.5220/0010350200002859.

Ambrosino, D., Asta, V., Bartoli, F., 2019. A comparison of optimization models to evaluate the impact of fuel costs when designing new cruise itineraries. In: A View of Operations Research Applications in Italy, 2018. Springer, pp. 179–190. http://dx.doi.org/10.1007/978-3-030-25842-9_14.

Ancona, M., Baldi, F., Bianchi, M., Branchini, L., Melino, F., Peretto, A., Rosati, J., 2018. Efficiency improvement on a cruise ship: Load allocation optimization. Energy Convers. Manage. 164, 42–58. http://dx.doi.org/10.1016/j.enconman.2018.02.080, URL https://www.sciencedirect.com/science/article/pii/S0196890418301973.

Asta, V., Ambrosino, D., Bartoli, F., 2018. An optimization model to design a new cruise itinerary: the case of costa crociere. IFAC-PapersOnLine 51 (9), 446–451. http://dx.doi.org/10.1016/j.ifacol.2018.07.073.

Baldi, F., Ahlgren, F., Nguyen, T.-V., Thern, M., Andersson, K., 2018. Energy and exergy analysis of a cruise ship. Energies 11 (10), 2508. http://dx.doi.org/10.3390/en11102508, URL https://www.mdpi.com/1996-1073/11/10/2508.

Bertagna, S., Kouznetsov, I., Braidotti, L., Marino, A., Bucci, V., 2023. A rational approach to the ecological transition in the cruise market: Technologies and design compromises for the fuel switch. J. Mar. Sci. Eng. 11, 67. http://dx.doi.org/10.3390/jmse11010067.

Blendermann, W., 2014. Book Review: Practical Ship and Offshore Structure Aerodynamics. Taylor & Francis, http://dx.doi.org/10.1179/str.2014.61.2.004.

Bouman, E.A., Lindstad, E., Rialland, A.I., Strømman, A.H., 2017. State-of-the-art technologies, measures, and potential for reducing GHG emissions from shipping – A review. Transp. Res. D 52, 408–421. http://dx.doi.org/10.1016/j.trd.2017.03.022.

Bouman, E.A., Lindstad, H.E., Stromman, A.H., 2016. Life-cycle approaches for bottom-up assessment of environmental impacts of shipping. In: SNAME Maritime Convention. Day 4 Fri, November 04, 2016, D043S018R003.

Bowman, A.W., Azzalini, A., 1997. Applied Smoothing Techniques for Data Analysis: The Kernel Approach with S-Plus Illustrations, vol. 18, OUP Oxford.

Braidotti, L., Bertagna, S., Rappoccio, R., Utzeri, S., Bucci, V., Marinò, A., 2023. On the inconsistency and revision of Carbon Intensity Indicator for cruise ships. Transp. Res. D 118, 103662. http://dx.doi.org/10.1016/j.trd.2023.103662.

Byrd, R.H., Gilbert, J.C., Nocedal, J., 2000. A trust region method based on interior point techniques for nonlinear programming. Math. Program. 89, 149–185. http://dx.doi.org/10.1007/PL00011391.

Byrd, R.H., Hribar, M.E., Nocedal, J., 1999. An interior point algorithm for large-scale nonlinear programming. SIAM J. Optim. 9 (4), 877–900. http://dx.doi.org/10.1137/S1052623497325107.

Coleman, T.F., Li, Y., 1994. On the convergence of reflective Newton methods for large-scale nonlinear minimization subject to bounds. Math. Program. 67 (2), 189–224. http://dx.doi.org/10.1007/BF01582221.

Coleman, T.F., Li, Y., 1996. An interior, trust region approach for nonlinear minimization subject to bounds. SIAM J. Optim. 6, 418–445.

Copernicus Marine Service, 2024. Copernicus marine environment monitoring service products. URL https://data.marine.copernicus.eu/products.

Donatini, L., Vantorre, M., Verwilligen, J., Delefortrie, G., 2019. Description of hydro/meteo data in ship manoeuvring simulators: A survey on the state of the art. Ocean Eng. 189, 106344. http://dx.doi.org/10.1016/j.oceaneng.2019.106344.

European Commission, 2021. 'Fit for 55': delivering the EU's 2030 climate target on the way to climate neutrality. In: Communication from the Commission to the European Parliament, the European Council, the Council, the European Economic and Social Committee and the Committee of the Regions. European Commission Brussels, Belgium.

Faltinsen, O.M., 1980. Prediction of resistance and propulsion of a ship in a seaway. In: 13th Symposium on Naval Hydrodynamics. Tokyo, pp. 505–529.

Fan, A., Yan, X., Bucknall, R., Yin, Q., Ji, S., Liu, Y., Song, R., Chen, X., 2020. A novel ship energy efficiency model considering random environmental parameters. J, Mar. Eng. Technol. 19 (4), 215–228. http://dx.doi.org/10.1080/20464177.2018.1546644.

Fan, A., Yang, J., Yang, L., Wu, D., Vladimir, N., 2022. A review of ship fuel consumption models. Ocean Eng. 264, 112405. http://dx.doi.org/10.1016/j.oceaneng.2022.112405.

Fossen, T.I., 2011. Handbook of Marine Craft Hydrodynamics and Motion Control. John Wiley & Sons, http://dx.doi.org/10.1002/9781119994138.

Fuentes García, G., Sosa Echeverría, R., Baldasano Recio, J.M., W. Kahl, J.D., Antonio Durán, R.E., 2022. Review of top-down method to determine atmospheric emissions in port. case of study: Port of Veracruz, Mexico. J. Mar. Sci. Eng. 10 (1), 96. http://dx.doi.org/10.3390/jmse10010096.

Hogben, N., Dacunha, N., Oliver, G., 1986. Global Wave Statistics. British Maritime Technology Limited.

Holtrop, J., Mennen, G., et al., 1982. An approximate power prediction method. Int. Shipbuild. Prog. 29 (335), 166–170. http://dx.doi.org/10.3233/ISP-1982-2933501.

IMO, 2018. Resolution MEPC.308(73) Adopted on 26 October 2018 - 2018 Guidelines on the Method of Calculation of the Attained Energy Efficiency Design Index (EEDI) for New Ships. Technical Report, International Maritime Organization.

IMO, 2020. Fourth IMO GHG Study 2020 Full Report. International Maritime Organization (IMO).

IMO, 2021a. Resolution MEPC.337(76) - 2021 Guidelines on the Reference Lines for the Use with Operational Carbon Intensity Indicators (CII Reference Lines Guidelines, G2). International Maritime Organization.

IMO, 2021b. Resolution MEPC.338(76) - 2021 Guidelines on the Operational Carbon Intensity Reduction Factor Relative to Reference Lines (CII Reduction Factors Guidelines, G3). Technical Report, International Maritime Organization.

IMO, 2021c. Resolution MEPC.339(76) - 2021 Guidelines on the Operational Carbon Intensity Rating of Ships (CII Rating Guidelines, G4). International Maritime Organization.

IMO, 2022. Resolution MEPC.352(78) Adopted on 10 June 2022 - 2022 Guidelines on Operational Carbon Intensity Indicators and the Calculation Methods (CII Guidelines, G1). Technical Report, International Maritime Organization.

IMO, 2023a. Resolution MEPC.376(80) Adopted on 7 July 2023 - 2023 Guidelines on Life Cycle GHG Intensity of Marine Fuels (LCA Guidelines). Technical Report, International Maritime Organization.

IMO, 2023b. Resolution MEPC.377(80) Adopted on 7 July 2023 - 2023 IMO Strategy on Reduction of GHG Emissions from Ships. Technical Report, International Maritime Organization.

Intergovernmental Oceanographic Commission, 2010. IOC, SCOR and IAPSO, 2010: the International thermodynamic equation of seawater, 2010: calculation and use of thermodynamic properties. In: Manuals and Guides, (vol. 56), UNESCO: United Nations Educational, Scientific and Cultural Organisation, p. 196.

ISO Ships, 2015. Marine Technology—Guidelines for the Assessment of Speed and Power Performance by Analysis of Speed Trial Data. ISO, Geneva, Switzerland.

ITTC, 1957. Eight international towing tank conference : Madrid, 15 - 23 september, 1957 ; proceedings.

ITTC, 2014. Recommended Procedures and Guidelines 7.5-04-01-01.2, Analysis of Speed/Power Trial Data. Technical Report.

Jeuring, J., Samuelsen, E.M., Lamers, M., Müller, M., Hjøllo, B.Å., Bertino, L., Hagen, B., 2024. Map-based ensemble forecasts for maritime operations: An interactive usability assessment with decision scenarios. Weather Clim. Soc. 16 (1), 235–256. http://dx.doi.org/10.1175/WCAS-D-23-0076.1, URL https://journals.ametsoc.org/view/journals/wcas/16/1/WCAS-D-23-0076.1.xml.

Jinkine, V., Ferdinande, V., 1974. A method for predicting the added resistance of fast cargo ships in head waves. Int. Shipbuild. Prog. 21 (238), 149–167. http://dx.doi.org/10.3233/ISP-1974-2123801.

Johansson, L., Jalkanen, J.-P., Kukkonen, J., 2017. Global assessment of shipping emissions in 2015 on a high spatial and temporal resolution. Atmos. Environ. 167, http://dx.doi.org/10.1016/j.atmosenv.2017.08.042.

Johnson, N.L., Kotz, S., Balakrishnan, N., 1995. Continuous univariate distributions, volume 2, vol. 289, John wiley & sons.

Kanellos, F.D., 2014. Optimal power management with GHG emissions limitation in all-electric ship power systems comprising energy storage systems. IEEE Trans. Power Syst. 29 (1), 330–339. http://dx.doi.org/10.1109/TPWRS.2013.2280064.

Kepaptsoglou, K., Fountas, G., Karlaftis, M.G., 2015. Weather impact on containership routing in closed seas: A chance-constraint optimization approach. Transp. Res. C 55, 139–155. http://dx.doi.org/10.1016/j.trc.2015.01.027.

Kitamura, F., Ueno, M., Fujiwara, T., Sogihara, N., 2017. Estimation of above water structural parameters and wind loads on ships. Ships Offshore Struct. 12 (8), 1100–1108. http://dx.doi.org/10.1080/17445302.2017.1316556.

Kobayashi, E., Hashimoto, H., Taniguchi, Y., Yoneda, S., 2015. Advanced optimized weather routing for an ocean-going vessel. In: 2015 International Association of Institutes of Navigation World Congress. IAIN, pp. 1–8. http://dx.doi.org/10.1109/IAIN.2015.7352247.

Kotz, N.J., Balakrishnan, N., 1993. Continuous Univariate Distributions, Vol. 1. Hoboken, Wiley Interssience, NJ.

Kramel, D., Muri, H., Kim, Y., Lonka, R., Nielsen, J.B., Ringvold, A.L., Bouman, E.A., Steen, S., Strømman, A.H., 2021. Global shipping emissions from a well-to-wake perspective: the MariTEAM model. Environ. Sci. Technol. 55 (22), 15040–15050. http://dx.doi.org/10.1021/acs.est.1c03937.

Kresic, M., Haskell, B., 1983. Effects of propeller design–point definition on the performance of a propeller. In: Diesel Engine System with Regard to in–Service Roughness, Weather Conditions. pp. 195–224.

Kuroda, M., Sugimoto, Y., 2022. Evaluation of ship performance in terms of shipping route and weather condition. Ocean Eng. 254, 111335. http://dx.doi.org/10.1016/j.oceaneng.2022.111335.

Kytariolou, A., Themelis, N., 2023. Optimized route planning under the effect of hull and propeller fouling and considering ocean currents. J. Mar. Sci. Eng. 11, 828. http://dx.doi.org/10.3390/jmse11040828.

Lackenby, H., 1963. The effect of shallow water on ship speed. Shipbuild. Mar. Eng. 70, 446–450. http://dx.doi.org/10.1111/j.1559-3584.1964.tb04413.x.

Lang, X., Mao, W., 2020. A semi-empirical model for ship speed loss prediction at head sea and its validation by full-scale measurements. Ocean Eng. 209, 107494. http://dx.doi.org/10.1016/j.oceaneng.2020.107494, URL https://www.sciencedirect.com/science/article/pii/S0029801820305072.

Lin, L.Y., Tsai, C.C., Lee, J.Y., 2022. A study on the trends of the global cruise tourism industry, sustainable development, and the impacts of the COVID-19 pandemic. Sustainability 14 (11), http://dx.doi.org/10.3390/su14116890.

Lindstad, E., Rialland, A., 2020. LNG and cruise ships, an easy way to fulfil regulations—Versus the need for reducing GHG emissions. Sustainability 12 (5), http://dx.doi.org/10.3390/su12052080.

Liu, S., Papanikolaou, A., 2020. Regression analysis of experimental data for added resistance in waves of arbitrary heading and development of a semi-empirical formula. Ocean Eng. 206, 107357. http://dx.doi.org/10.1016/j.oceaneng.2020.107357.

Malone, J., Little, D., 1980. Effects of Hull Foulants and Cleaning/Coating Practices on Ship Performance and Economics, vol. 88, Society of Naval Architects and Marine Engineers.

McDougall, T.J., Jackett, D.R., Wright, D.G., Feistel, R., 2003. Accurate and computationally efficient algorithms for potential temperature and density of seawater. J. Atmos. Ocean. Technol. 20 (5), 730–741. http://dx.doi.org/10.1175/1520-0426(2003)20<730:AACEAF>2.0.CO;2.

Merien-Paul, R.H., Enshaei, H., Jayasinghe, S.G., 2018. In-situ data vs. bottom-up approaches in estimations of marine fuel consumptions and emissions. Transp. Res. D 62, 619–632. http://dx.doi.org/10.1016/j.trd.2018.04.014.

Molland, A.F. (Ed.), 2008. Chapter 5 - powering. The Maritime Engineering Reference Book. Butterworth-Heinemann, Oxford, pp. 181–343. http://dx.doi.org/10.1016/B978-0-7506-8987-8.00005-6.

Molland, A.F., Turnock, S.R., 2011. Marine Rudders and Control Surfaces: Principles Data Design and Applications. Elsevier.

Moré, J.J., Garbow, B.S., Hillstrom, K.E., 1980. User guide for MINPACK-1. Technical Report CM-P00068642.

Moskowitz, L., Pierson, W., Mehr, E., 1962-63. Wave spectra estimated from wave records obtained by the OWS weather explorer and OWS weather reporter.

Muri, H., Strømman, A.H., Ringvold, A.L., Lonka, R., Lindstad, E., Bouman, E.A., 2019. A new emission inventory of the global maritime fleet; the effect of weather. In: AGU Fall Meeting Abstracts, Vol. 2019. pp. A21W–2637.

NGIA, 2024. World Port Index - National Geospatial-Intelligence Agency. URL https://msi.nga.mil/Publications/APC.

Nocedal, J., Öztoprak, F., Waltz, R.A., 2014. An interior point method for nonlinear programming with infeasibility detection capabilities. Optim. Methods Softw. 29 (4), 837–854. http://dx.doi.org/10.1080/10556788.2013.858156.

Nunes, R., Alvim-Ferraz, M., Martins, F., Sousa, S., 2017. The activity-based methodology to assess ship emissions - A review. Environ. Pollut. 231, 87–103. http://dx.doi.org/10.1016/j.envpol.2017.07.099.

Osinski, R.D., Radtke, H., 2020. Ensemble hindcasting of wind and wave conditions with WRF and WAVEWATCH III® driven by ERA5. Ocean Sci. 16 (2), 355–371. http://dx.doi.org/10.5194/os-16-355-2020.

Powell, M.J., 1968. A Fortran Subroutine for Solving Systems of Nonlinear Algebraic Equations. Technical Report, Atomic Energy Research Establishment, Harwell, England, United Kingdom.

Roquet, F., Madec, G., McDougall, T.J., Barker, P.M., 2015. Accurate polynomial expressions for the density and specific volume of seawater using the TEOS-10 standard. Ocean Model. 90, 29–43. http://dx.doi.org/10.1016/j.ocemod.2015.04.002.

Sandvik, E., Nielsen, J.B., Asbjørnslett, B.E., Eilif, P., Fagerholt, K., 2021. Operational sea passage scenario generation for virtual testing of ships using an optimization for simulation approach. J. Mar. Sci. Technol. 26, 896–916. http://dx.doi.org/10.1007/s00773-020-00771-0.

Schwarzkopf, D.A., Petrik, R., Matthias, V., Quante, M., Majamäki, E., Jalkanen, J.P., 2021. A ship emission modeling system with scenario capabilities. Atm. Environ. X 12, 100132. http://dx.doi.org/10.1016/j.aeaoa.2021.100132.

Simonsen, M.H., Larsson, E., Mao, W., Ringsberg, J.W., 2015. State-of-the-art within ship weather routing. In: International Conference on Offshore Mechanics and Arctic Engineering, Vol. 56499. American Society of Mechanical Engineers, V003T02A053. http://dx.doi.org/10.1115/OMAE2015-41939.

Sucheran, R., 2021. Global impacts and trends of the COVID-19 pandemic on the cruise sector: A focus on South Africa. Afr. J. Hosp. Tour. Leis. 10 (1), http://dx.doi.org/10.46222/ajhtl.19770720-84.

Tadros, M., Ventura, M., Guedes Soares, C., 2023. Effect of hull and propeller roughness during the assessment of ship fuel consumption. J. Mar. Sci. Eng. 11 (4), 784. http://dx.doi.org/10.3390/jmse11040784.

Tadros, M., Vettor, R., Ventura, M., Guedes Soares, C., 2022. Assessment of ship fuel consumption for different hull roughness in realistic weather conditions. J. Mar. Sci. Eng. 10 (12), 1891. http://dx.doi.org/10.3390/jmse10121891.

Tillig, F., Ringsberg, J.W., 2019. A 4 DOF simulation model developed for fuel consumption prediction of ships at sea. Ships Offshore Struct. 14 (sup1), 112–120. http://dx.doi.org/10.1080/17445302.2018.1559912.

Toscano, D., Murena, F., 2019. Atmospheric ship emissions in ports: A review. Correlation with data of ship traffic. Atm. Environ. X 4, 100050. http://dx.doi.org/10.1016/j.aeaoa.2019.100050.

Townsin, R., Byrne, D., 1980. Speed, Power and Roughness: The Economics of Outer Bottom Maintenance. vol. 122, Society of Naval Architects and Marine Engineers.

TuTiempo, 2024. Climate of the world: Weather history and climate data. URL https://en.tutiempo.net/climate/ws-165220.html.

Uzun, D., Demirel, Y., Coraddu, A., Turan, O., 2019. Time-dependent biofouling growth model for predicting the effects of biofouling on ship resistance and powering. Ocean Eng. 191, http://dx.doi.org/10.1016/j.oceaneng.2019.106432.

Van Oortmerssen, G., 1971. A power prediction method and its application to small ships. Int. Shipbuild. Prog. 18 (207), 397–415. http://dx.doi.org/10.3233/ISP-1971-1820701.

Vasilikis, N., Geertsma, R., Visser, K., 2022. Operational data-driven energy performance assessment of ships: the case study of a naval vessel with hybrid propulsion. J, Mar. Eng. Technol. 22, 1–17. http://dx.doi.org/10.1080/20464177.2022.2058690.

Vettor, R., Guedes Soares, C., 2022. Reflecting the uncertainties of ensemble weather forecasts on the predictions of ship fuel consumption. Ocean Eng. 250, 111009. http://dx.doi.org/10.1016/j.oceaneng.2022.111009.

Waltz, R.A., Morales, J.L., Nocedal, J., Orban, D., 2006. An interior algorithm for nonlinear optimization that combines line search and trust region steps. Math. Program. 107 (3), 391–408. http://dx.doi.org/10.1007/s10107-004-0560-5.

Wang, K., Wang, J., Huang, L., Yuan, Y., Wu, G., Xing, H., Wang, Z., Wang, Z., Jiang, X., 2022. A comprehensive review on the prediction of ship energy consumption and pollution gas emissions. Ocean Eng. 266, 112826. http://dx.doi.org/10.1016/j.oceaneng.2022.112826.

Wärtsilä, 2024. Engines and Generating Sets, URL https://www.wartsila.com/marine/products/engines-and-generating-sets.

Woo, D., Im, N., 2021. Spatial analysis of the ship gas emission inventory in the port of busan using bottom-up approach based on AIS data. J. Mar. Sci. Eng. 9 (12), 1457. http://dx.doi.org/10.3390/jmse9121457.

Zaccone, R., Ottaviani, E., Figari, M., Altosole, M., 2018. Ship voyage optimization for safe and energy-efficient navigation: A dynamic programming approach. Ocean Eng. 153, http://dx.doi.org/10.1016/j.oceaneng.2018.01.100.

Zis, T.P., Psaraftis, H.N., Ding, L., 2020. Ship weather routing: A taxonomy and survey. Ocean Eng. 213, 107697. http://dx.doi.org/10.1016/j.oceaneng.2020.107697.